Icarus 220 (2012) 36–50

Contents lists available at SciVerse ScienceDirect

Icarus

journal homepage: www.elsevier.com/locate/icarus

# Phase reddening on near-Earth asteroids: Implications for mineralogical analysis, space weathering and taxonomic classification

Juan A. Sanchez [a,b,*], Vishnu Reddy [a,c,1], Andreas Nathues [a,1], Edward A. Cloutis [d], Paul Mann [d], Harald Hiesinger [b]

[a] Max Planck Institut für Sonnensystemforschung, Max Planck Str. 2, 37191 Katlenburg-Lindau, Germany
[b] Institut für Planetologie, 48149 Münster, Germany
[c] Department of Space Studies, University of North Dakota, Grand Forks, ND 58202, USA
[d] Department of Geography, University of Winnipeg, Winnipeg, Manitoba, Canada

ARTICLE INFO

*Article history:*
Received 22 February 2012
Revised 2 April 2012
Accepted 2 April 2012
Available online 25 April 2012

*Keywords:*
Asteroids
Near-Earth objects
Spectroscopy
Infrared observations
Meteorites

ABSTRACT

Phase reddening is an effect that produces an increase of the spectral slope and variations in the strength of the absorption bands as the phase angle increases. In order to understand its effect on spectroscopic observations of asteroids, we have analyzed the visible and near-infrared spectra (0.45–2.5 μm) of 12 near-Earth asteroids observed at different phase angles. All these asteroids are classified as either S-complex or Q-type asteroids. In addition, we have acquired laboratory spectra of three different types of ordinary chondrites at phase angles ranging from 13° to 120°. We have found that both, asteroid and meteorite spectra show an increase in band depths with increasing phase angle. In the case of the asteroids the Band I depth increases in the range of $\sim 2° < g < 70°$ and the Band II depth increases in the range of $\sim 2° < g < 55°$. Using this information we have derived equations that can be used to correct the effect of phase reddening in the band depths. Of the three meteorite samples, the (olivine-rich) LL6 ordinary chondrite is the most affected by phase reddening. The studied ordinary chondrites have their maximum spectral contrast of Band I depths at a phase angle of ~60°, followed by a decrease between 60° and 120° phase angle. The Band II depths of these samples have their maximum spectral contrast at phase angles of 30–60° which then gradually decreases to 120° phase angle. The spectral slope of the ordinary chondrites spectra shows a significant increase with increasing phase angle for $g > 30°$. Variations in band centers and band area ratio (BAR) values were also found, however they seems to have no significant impact on the mineralogical analysis. Our study showed that the increase in spectral slope caused by phase reddening is comparable to certain degree of space weathering. In particular, an increase in phase angle in the range of 30–120° will produce a reddening of the reflectance spectra equivalent to exposure times of $\sim 0.1 \times 10^6$–$1.3 \times 10^6$ years at about 1 AU from the Sun. This increase in spectral slope due to phase reddening is also comparable to the effects caused by the addition of different fractions of SMFe. Furthermore, we found that under some circumstances phase reddening could lead to an ambiguous taxonomic classification of asteroids.



## 1. Introduction

Near-infrared (NIR) spectroscopy is a powerful technique to derive information about the surface mineralogy of asteroids. This mineralogical characterization relies primarily on the identification and analysis of diagnostic features present in the spectra of some asteroids. Olivine and pyroxene are two common mafic minerals found on asteroids (Gaffey et al., 2002), and their spectral properties dominate the reflectance spectra of some particular classes. Asteroids belonging to the S-complex and Q-types (DeMeo et al., 2009, Bus–DeMeo taxonomy hereafter) are examples of these objects. In the case of olivine, the absorption feature is composed of three overlapping bands and is centered near 1.04–1.1 μm, while pyroxenes show to major absorption bands, centered near 0.9–1 μm and 1.9–2 μm, all of them caused by the presence of $Fe^{2+}$ cations (e.g., Adams, 1974, 1975; Burns, 1993). In the spectra of olivine–pyroxene mixtures the wavelength position (band centers) of the combined absorption features near 1 μm (Band I) is a function of relative abundance and composition of olivine and pyroxene, while the position of the feature near 2 μm (Band

* Corresponding author at: Max Planck Institut für Sonnensystemforschung, Max Planck Str. 2, 37191 Katlenburg-Lindau, Germany.
*E-mail address:* sanchez@mps.mpg.de (J.A. Sanchez).

[1] Visiting Astronomer at the Infrared Telescope Facility, which is operated by the University of Hawaii under Cooperative Agreement No. NNX-08AE38A with the National Aeronautics and Space Administration, Science Mission Directorate, Planetary Astronomy Program.

0019-1035/$ - see front matter © 2012 Elsevier Inc. All rights reserved.
http://dx.doi.org/10.1016/j.icarus.2012.04.008

II) is a function of the pyroxene composition (Cloutis et al., 1986; Gaffey et al., 1993). In addition to the absorption band centers, the ratio of the area of Band II to that of Band I, known as band area ratio (BAR), is used to estimate olivine and pyroxene abundances in asteroids and meteorites (Cloutis et al., 1986; Burbine et al., 2003; Dunn et al., 2010). Together, these spectral band parameters constitute a useful tool to obtain information about the surface mineralogy and composition of asteroids. However, band parameters can also be affected by other factors not related to compositional variations. One of these factors is the phase angle at the moment of the observation. The phase angle ($g$), is defined as the angular separation between the Sun and the observer as seen from the target. Phase angle induced effects can manifest themselves as phase reddening, which produces an artificial increase (reddening) of the spectral slope and variations in the strength of the absorption bands with increasing phase angle. This effect is explained as the result of the wavelength dependence of the single-scattering albedo (Gradie et al., 1980; Gradie and Veverka, 1986; Clark et al., 2002b). Traditionally, the term phase reddening was used to describe only the increase of the spectral slope or continuum, however as will be shown later, as the phase angle increases variations in the absorption bands are also seen. Therefore, in the present work the term phase reddening is extended to refer not only to the increase of the spectral slope, but also to the variations in the strength of the absorption bands.

Phase reddening effect among Solar System objects was first noticed in asteroid broad band colors. Gehrels (1970) reported a phase reddening in the B-V and U-B colors of 4 Vesta to be 0.0018 and 0.0027 mag/degree, respectively. Additional studies using photometric observations include the works of Millis et al. (1976) and Lumme and Bowell (1981). The effects of phase reddening have been also observed among NEAs. Luu and Jewitt (1990) found that the spectral slopes of NEAs in general are higher than those measured for 3:1 resonance asteroids. Since NEAs are often observed at high phase angles this increase in the spectral slopes was interpreted as phase reddening.

Nathues (2000, 2010) carried out a spectroscopic and spectrophotometric survey of the Eunomia asteroid family, obtaining spectra in visible (VIS) and NIR wavelengths of 97 of its members. The analysis of the spectral slopes of these asteroids revealed an average increase of 0.067%/100 nm per degree with increasing phase angle in the range of $2^\circ < g < 24^\circ$. Apart from the increase of the spectral slope he also observed an increase of the 1 μm absorption band (depth) with increasing phase angle.

Reddy et al. (2012) conducted an extensive study of Asteroid (4) Vesta in order to quantify phase angle-induced spectral effects on this asteroid prior to the arrival of the Dawn spacecraft. Rotationally resolved NIR spectral observations (0.7–2.5 μm) were obtained for this purpose. They found that in the phase angle range of $0^\circ < g \leqslant 25^\circ$ for every 10° increase in phase angle, Vesta's Band I and Band II depths increase 2.35% and 1.5%, respectively, and the BAR value increases by 0.30.

Phase reddening effect has been also detected and quantified from spacecraft observations of asteroids. The NEAR Shoemaker spacecraft obtained NIR spectroscopic observations (0.8–2.4 μm) of Asteroid (433) Eros at phase angles ranging from 0° to 100°. These observations showed the most intense phase reddening for wavelengths inside of the 1.0 μm band, occurring at the level of 10% across this phase angle range (Clark et al., 2002b; Bell et al., 2002). Similar results were observed from NIR reflectance spectra of Asteroid (25143) Itokawa acquired by the Hayabusa spacecraft (Kitazato et al., 2008).

Laboratory measurements of different materials have confirmed the existence of the phase reddening effect. Gradie et al. (1980) investigated phase angle induced effects on the spectrophotometric properties of powdered materials. They obtained reflectance spectra at phase angles of $4^\circ \leqslant g \leqslant 120^\circ$, in the wavelength range $0.4 \leqslant \lambda \leqslant 1.2$ μm. All the samples studied by them showed a significant reddening as the phase angle increases from 4° to 120°. Furthermore, some of the spectra showed variations in the spectral contrast of the absorption bands with increasing phase angle. More recent laboratory studies related to phase reddening include the works of Mann et al. (2011) and Shepard and Cloutis (2011).

Despite the fact that phase reddening has been known for a long time, its effect on the analysis of asteroid spectra has not been fully assessed. In the present work we study the phase reddening on NEAs and its implications for mineralogical analysis, space weathering and taxonomic classification. Due to their proximity, NEAs can exhibit a wide range of phase angles, often much higher than those observed for main belt asteroids, which make them the logical choice for this study. Our investigation focuses on the analysis of 27 VIS–NIR spectra of 12 NEAs previously classified as either S-complex or Q-types (Bus–DeMeo), which have been observed at different phase angles. In addition to the ground-based observations, laboratory spectra of ordinary chondrites are also analyzed and the results compared to those obtained from the asteroid spectral data.

## 2. Phase reddening from ground-based observations of NEAs

### 2.1. The data

One of the drawbacks of this kind of study is the necessity to obtain multiple observations of the same asteroids at different phase angles, which in terms of allocated observation time can be very difficult to do. For this reason we have decided to combine data from Reddy (2009), DeMeo et al. (2009), Abell et al. (2007), Binzel et al. (2001) and the MIT-UH-IRTF Joint Campaign for NEO Spectral Reconnaissance (NEOSR). All of these observations were conducted with the SpeX instrument (Rayner et al., 2003) on the NASA Infrared Telescope Facility (IRTF). The NIR spectra (0.7–2.5 μm) were obtained using Spex in its low resolution ($R \sim 150$) prism mode with a 0.8″ slit width. Typical observations consist of acquiring frames employing a nodding sequence in which the object is alternated between two different slit positions (A and B) following the sequence ABBA. Since the object and the sky are observed simultaneously in each exposure, by subtracting A from B and B from A, is possible to remove the sky background during the data reduction process. In order to minimize the effects of differential atmospheric refraction the slit is oriented along the parallactic angle during the observations. To correct for telluric water vapor features, and to obtain the relative reflectance, local standard and solar analog stars are observed at airmasses as similar as possible as the asteroids. Flat fields and arc line spectra for each night are also obtained during the observations. The data reduction is performed using different packages, including IRAF and Spextool (Cushing et al., 2004). For more details about the observing protocols and reduction of these data sets see Reddy (2009), DeMeo et al. (2009), Abell et al. (2007) and Binzel et al. (2001). The spectra of the NEAs at visible wavelengths used in the present work were taken from Binzel et al. (2001, 2004) and DeMeo et al. (2009). All the spectra were normalized to unity at 0.55 μm. Observational circumstances for the studied objects are presented in Table 1.

### 2.2. Spectral band analysis of NEAs

As mentioned earlier, increasing the phase angle will produce an increase in the spectral slope and changes in the strength of the absorption bands. Spectral slope variations can be interpreted as surface heterogeneities caused by different factors such as metal

**Table 1**
NEAs observational circumstances. The columns in this table are: object number and designation, UT date of observation, the phase angle ($g$) and the heliocentric distance at the time of observation.

| Object | UT date | $g$ (°) | Heliocentric distance (AU) |
|---|---|---|---|
| 1036 Ganymed[a] | 09–March–2005 | 5.9 | 4.09 |
| 1036 Ganymed[b] | 01–June–2006 | 15.2 | 3.01 |
| 1620 Geographos[b] | 10–March–2008 | 38.3 | 1.09 |
| 1620 Geographos[c] | 27–February–2008 | 12.0 | 1.16 |
| 1620 Geographos[a] | 29–January–2001 | 16.7 | 1.39 |
| 1627 Ivar[b] | 02–October–2008 | 31.0 | 1.58 |
| 1627 Ivar[b] | 03–December–2008 | 16.0 | 1.90 |
| 1862 Apollo[b] | 13–November–2005 | 51.7 | 1.05 |
| 1862 Apollo[b] | 22–November–2005 | 15.4 | 1.20 |
| 1980 Tezcatlipoca[b] | 25–October–2006 | 54.6 | 1.17 |
| 1980 Tezcatlipoca[c] | 05–January–2007 | 25.0 | 1.48 |
| 4179 Toutatis[b] | 15–September–2004 | 27.0 | 1.09 |
| 4179 Toutatis[b] | 02–October–2008 | 68.0 | 1.06 |
| 4179 Toutatis[c] | 13–August–2008 | 6.1 | 1.45 |
| 4954 Eric[b] | 20–July–2007 | 28.3 | 1.67 |
| 4954 Eric[c] | 26–November–2007 | 62.0 | 1.10 |
| 6239 Minos[a] | 26–January–2004 | 47.3 | 1.03 |
| 6239 Minos[b] | 06–September–2010 | 2.4 | 1.20 |
| 11398[b] | 10–March–2008 | 33.0 | 1.16 |
| 11398[c] | 28–February–2008 | 19.0 | 1.21 |
| 25143 Itokawa[d] | 12–March–2001 | 25.6 | 1.07 |
| 25143 Itokawa[e] | 28–March–2001 | 69.0 | 1.01 |
| 35107[c] | 26–July–2008 | 87.0 | 1.08 |
| 35107[a] | 27–December–2002 | 45.0 | 1.20 |
| 66146[b] | 02–October–2008 | 70.3 | 1.06 |
| 66146[b] | 13–October–2010 | 32.1 | 1.15 |
| 66146[b] | 06–September–2010 | 55.3 | 1.16 |

[a] Data from DeMeo et al. (2009).
[b] Data from NEOSR, http://smass.mit.edu/minus.html.
[c] Data from Reddy (2009).
[d] Data from Abell et al. (2007).
[e] Data from Binzel et al. (2001).

content, particle size and space weathering (Gaffey et al., 1993; Clark et al., 2002a; Gaffey, 2010). However, this parameter is also known to be very sensitive to other factors. Apart from the viewing geometry, atmospheric differential refraction (Filippenko, 1982), airmass differences between the standard star and the asteroid at the time of the observations (DeMeo et al., 2011), incorrect centering of the object in the slit (Cushing et al., 2004), poor weather conditions (Bus et al., 2002) and the use of different solar analogs (Sunshine et al., 2004) are often the cause of fluctuations in the asteroid's spectral slope. In some cases the origin of these error sources is difficult to determine since they are seen as nonsystematic variations in the final asteroid reflectance spectrum (Hardersen et al., 2006). Therefore, in order to better quantify the effect of phase reddening on the spectral slope we will leave that part of the study to the laboratory spectra (see Section 3), and will focus our attention on the analysis of the absorption bands of the asteroid spectra.

The spectral band parameters for each VIS–NIR spectrum were measured using the Spectral Processing Routine (SpecPR) program based on the protocols discussed by Cloutis et al. (1986), Gaffey et al. (2002), and Gaffey (2003). Band centers are calculated by dividing out the linear continuum and fitting an n-order polynomial over the bottom third of each band. In the case of Band II, we defined the unresolved red edge as 2.44 μm. After ratioing the absorption features to the straight-line continuum, a subroutine in SpecPR was used to calculate the band areas (areas between the linear continuum and the data curve) and band depths (measured from the continuum to the band center and given as percentage depths). The band areas were then used to calculate the BAR values. Each band parameter was measured 10 times using different order polynomial fits (typically third and fourth order) and sampling different ranges of points within the corresponding intervals. Averages of these measurements were taken as the final values. The uncertainties are given by the average $1-\sigma$ (standard deviation of the mean) calculated from the multiple measurements of each band parameter. The olivine–pyroxene abundance ratio of the asteroids was estimated using the relationship between $ol/(ol+px)$ and BAR derived by Dunn et al. (2010) from the analysis of 48 ordinary chondrite samples. This linear regression is expressed as

**Table 2**
NEAs spectral band parameters and their errors. The columns in this table correspond to: object number and designation, the phase angle ($g$), the average surface temperature ($T$), the Band I center (BI ± 0.01), the Band I depth ($BI_{dep}$ ± 0.3), the Band II center (BII ± 0.03), the temperature corrected Band II center (ΔBII ± 0.03), the Band II depth ($BII_{dep}$ ± 0.5), the temperature corrected Band II depth ($\Delta BII_{dep}$ ± 0.5), the band area ratio (BAR ± 0.04) and the temperature corrected band area ratio (ΔBAR ± 0.04).

| Object | $g$ (°) | $T$ (K) | BI (μm) | $BI_{dep}$ (%) | BII (μm) | ΔBII (μm) | $BII_{dep}$ (%) | $\Delta BII_{dep}$ (%) | BAR | ΔBAR |
|---|---|---|---|---|---|---|---|---|---|---|
| 1036 Ganymed | 5.9 | 129.6 | 0.909 | 18.79 | 1.867 | 1.901 | 8.05 | 5.49 | 0.901 | 0.768 |
| 1036 Ganymed | 15.2 | 150.9 | 0.917 | 18.22 | 1.883 | 1.913 | 9.29 | 7.05 | 1.101 | 0.984 |
| 1620 Geographos | 12.0 | 240.4 | 0.995 | 16.34 | 1.970 | 1.982 | 5.68 | 4.79 | 0.497 | 0.447 |
| 1620 Geographos | 16.7 | 219.6 | 0.997 | 16.77 | 1.967 | 1.984 | 6.56 | 5.35 | 0.490 | 0.425 |
| 1620 Geographos | 38.3 | 247.7 | 1.001 | 18.03 | 2.013 | 2.023 | 4.19 | 3.40 | 0.278 | 0.234 |
| 1627 Ivar | 16.0 | 198.9 | 0.948 | 19.14 | 1.955 | 1.975 | 6.26 | 4.74 | 0.407 | 0.326 |
| 1627 Ivar | 31.0 | 218.4 | 0.959 | 20.28 | 1.964 | 1.980 | 5.04 | 3.82 | 0.253 | 0.186 |
| 1862 Apollo | 15.4 | 243.3 | 0.986 | 25.00 | 1.997 | 2.008 | 4.81 | 3.96 | 0.188 | 0.141 |
| 1862 Apollo | 51.7 | 260.0 | 0.988 | 27.54 | 1.989 | 1.997 | 6.53 | 5.93 | 0.260 | 0.225 |
| 1980 Tezcatlipoca | 25.0 | 218.6 | 0.947 | 16.05 | 1.932 | 1.949 | 6.62 | 5.40 | 0.526 | 0.460 |
| 1980 Tezcatlipoca | 54.6 | 246.2 | 0.950 | 20.45 | 1.946 | 1.956 | 4.37 | 3.56 | 0.228 | 0.183 |
| 4179 Toutatis | 6.1 | 222.3 | 0.943 | 14.91 | 1.971 | 1.987 | 4.89 | 3.72 | 0.551 | 0.487 |
| 4179 Toutatis | 27.0 | 256.9 | 0.951 | 17.44 | 1.973 | 1.981 | 7.29 | 6.64 | 0.524 | 0.487 |
| 4179 Toutatis | 68.0 | 260.5 | 0.952 | 18.04 | 1.962 | 1.970 | 6.90 | 6.31 | 0.487 | 0.452 |
| 4954 Eric | 28.3 | 207.1 | 0.929 | 18.74 | 1.925 | 1.944 | 9.78 | 8.39 | 1.073 | 0.998 |
| 4954 Eric | 62.0 | 255.2 | 0.923 | 16.69 | 1.946 | 1.955 | 8.81 | 8.14 | 0.917 | 0.878 |
| 6239 Minos | 2.4 | 244.1 | 0.994 | 16.56 | 2.030 | 2.041 | 4.03 | 3.19 | 0.239 | 0.192 |
| 6239 Minos | 47.3 | 263.2 | 0.993 | 19.02 | 2.010 | 2.017 | 6.10 | 5.55 | 0.348 | 0.315 |
| 11398 | 19.0 | 243.3 | 0.913 | 19.04 | 1.935 | 1.946 | 6.89 | 6.04 | 0.622 | 0.575 |
| 11398 | 33.0 | 248.3 | 0.925 | 19.81 | 1.945 | 1.955 | 8.33 | 7.55 | 0.653 | 0.610 |
| 25143 Itokawa | 25.6 | 229.2 | 0.988 | 17.02 | 2.017 | 2.030 | 6.07 | 5.01 | 0.448 | 0.390 |
| 25143 Itokawa | 69.0 | 235.2 | 0.982 | 19.85 | 2.017 | 2.030 | 5.45 | 4.48 | 0.395 | 0.341 |
| 35107 | 45.0 | 244.1 | 0.984 | 19.57 | 2.019 | 2.030 | 7.40 | 6.56 | 0.452 | 0.405 |
| 35107 | 87.0 | 257.6 | 0.997 | 18.90 | 1.996 | 2.004 | 6.92 | 6.28 | 0.444 | 0.407 |
| 66146 | 32.1 | 250.1 | 0.992 | 22.17 | 1.983 | 1.993 | 6.20 | 5.45 | 0.339 | 0.296 |
| 66146 | 55.3 | 249.1 | 0.987 | 22.99 | 1.984 | 1.994 | 6.35 | 5.59 | 0.290 | 0.246 |
| 66146 | 70.3 | 260.2 | 0.986 | 22.57 | 1.992 | 2.000 | 5.75 | 5.15 | 0.306 | 0.272 |

**Table 3**
Olivine abundance with its error and taxonomy for the NEAs. The columns in this table are: object number and designation, the phase angle ($g$), the olivine–pyroxene abundance ratio ($ol/(ol+px) \pm 0.03$), the temperature corrected olivine–pyroxene ratio ($\Delta ol/(ol+px) \pm 0.03$), taxonomic classification (Bus–DeMeo) and principal components PC1′ and PC2′ for each asteroid.

| Object | $g$ (°) | $ol/(ol+px)$ | $\Delta ol/(ol+px)$ | Taxonomy | PC1′ | PC2′ |
|---|---|---|---|---|---|---|
| 1036 Ganymed | 5.9 | 0.51 | 0.54 | S | 0.2400 | 0.0416 |
| 1036 Ganymed | 15.2 | 0.46 | 0.49 | Sr | 0.3957 | 0.0381 |
| 1620 Geographos | 12.0 | 0.61 | 0.62 | Sq | −0.1096 | 0.0038 |
| 1620 Geographos | 16.7 | 0.61 | 0.63 | S | −0.0169 | 0.0206 |
| 1620 Geographos | 38.3 | 0.66 | 0.67 | Sqw | −0.2337 | 0.0503 |
| 1627 Ivar | 16.0 | 0.63 | 0.65 | S | −0.0151 | 0.0517 |
| 1627 Ivar | 31.0 | 0.67 | 0.68 | Sw | −0.0591 | 0.0689 |
| 1862 Apollo | 15.4 | 0.68 | 0.69 | Q | −0.5926 | 0.1996 |
| 1862 Apollo | 51.7 | 0.66 | 0.67 | Q | −0.6011 | 0.2387 |
| 1980 Tezcatlipoca | 25.0 | 0.60 | 0.62 | Sw | 0.1132 | 0.0508 |
| 1980 Tezcatlipoca | 54.6 | 0.67 | 0.68 | Sw | −0.0238 | 0.0588 |
| 4179 Toutatis | 6.1 | 0.59 | 0.61 | Sqw | −0.2825 | 0.0972 |
| 4179 Toutatis | 27.0 | 0.60 | 0.61 | Sq | −0.3115 | 0.1622 |
| 4179 Toutatis | 68.0 | 0.61 | 0.62 | Sq | −0.3278 | 0.1282 |
| 4954 Eric | 28.3 | 0.47 | 0.49 | Sw | 0.1552 | 0.0433 |
| 4954 Eric | 62.0 | 0.51 | 0.52 | Sr | 0.4719 | −0.0369 |
| 6239 Minos | 2.4 | 0.67 | 0.68 | Sq | −0.2907 | 0.0557 |
| 6239 Minos | 47.3 | 0.64 | 0.65 | Sqw | −0.3090 | 0.1231 |
| 11398 | 19.0 | 0.58 | 0.59 | Sr | 0.0631 | 0.0978 |
| 11398 | 33.0 | 0.57 | 0.58 | Sr | 0.1312 | 0.0912 |
| 25143 Itokawa | 25.6 | 0.62 | 0.63 | Sq | −0.3425 | 0.0946 |
| 25143 Itokawa | 69.0 | 0.63 | 0.65 | Sqw | −0.3283 | 0.1579 |
| 35107 | 45.0 | 0.62 | 0.63 | Sq | −0.2848 | 0.1281 |
| 35107 | 87.0 | 0.62 | 0.63 | Sq | −0.3077 | 0.1182 |
| 66146 | 32.1 | 0.65 | 0.66 | Q | −0.5262 | 0.1994 |
| 66146 | 55.3 | 0.66 | 0.67 | Q | −0.5737 | 0.1824 |
| 66146 | 70.3 | 0.65 | 0.66 | Q | −0.4978 | 0.1938 |

$$ol/(ol+px) = -0.242 \times \mathrm{BAR} + 0.728 \quad (1)$$

where the $ol/(ol+px)$ is expressed as a decimal. The band parameters and $ol/(ol+px)$ ratios with their corresponding errors obtained for each asteroid at different phase angles are presented in Tables 2 and 3 respectively.

### 2.3. Temperature correction to band parameters

Temperature-induced effects on the spectra of mafic minerals are characterized by shifting the band centers and broadening or narrowing the absorption features (Singer and Roush, 1985; Schade and Wäsch, 1999; Moroz et al., 2000; Hinrichs and Lucey, 2002). While surface temperature variations are considered of minor importance for main-belt asteroids, they may be significant for objects with higher eccentric orbits like NEAs (Moroz et al., 2000; Shestopalov and Golubeva, 2000). Furthermore, the spectra of laboratory samples are commonly obtained at room temperature (~300 K). Thus, in order to compare the band parameters with those measured for laboratory samples temperature corrections should be applied.

For each asteroid we have determined the average surface temperature ($T$) in the same way as (e.g., Burbine et al., 2009), where the temperature of the asteroid is approximated by the equation for energy conservation. The calculated temperatures of the NEAs are given in Table 2.

Since all the asteroids studied in this work are S-complex or Q-types, i.e., olivine–orthopyroxene assemblages, we have derived temperature corrections based on the analysis of ordinary chondrites. These meteorites are the most common type of meteorite to fall on Earth (~85% of all), and they have been generally linked to either S-complex or Q-type asteroids (e.g., Gaffey et al., 1993; Vernazza et al., 2008; Nakamura et al., 2011).

We have reanalyzed spectra of two H5 ordinary chondrites from Hinrichs and Lucey (2002) acquired in the temperature range between 80 and 400 K. Spectral band parameters (band centers, band depths and BAR) and their uncertainties were measured using the same methods applied to the asteroid spectra. These data were combined with the results obtained by Moroz et al. (2000) for a L5 and a LL4 ordinary chondrite acquired at temperatures between 293 and 80 K.

We found that Band II is the most affected by temperature variations. A correlation between Band II centers and temperature is observed for all samples, i.e., Band II centers shift to longer wavelengths as the temperature increases. Therefore, to each data set a linear fit was performed and the equations that represent those linear fits were averaged, obtaining the following expression:

$$\mathrm{BII}(T) = 0.0002 \times T\ (\mathrm{K}) + 1.87 \quad (2)$$

where the Band II center (BII) is given in μm. From this equation we derived a wavelength correction for the Band II center

$$\Delta\mathrm{BII}\ (\mu\mathrm{m}) = 0.06 - 0.0002 \times T\ (\mathrm{K}) \quad (3)$$

This correction is derived with respect to room temperature (300 K) and must be added to the calculated Band II center of each asteroid. The temperature corrected Band II centers are presented in Table 2. For the Band I center we found that the wavelength shift is in general very small (~0.003 μm), so no temperature correction was derived.

A decrease in Band II depth with increasing temperature was found for the three groups of ordinary chondrites. No obvious trend was observed for the Band I depth. Applying a similar procedure to the Band II center, we can estimate the approximate rate of change of the Band II depth for a range of temperatures

$$\mathrm{BII}_{dep}(T) = 20.89 - 0.015 \times T\ (\mathrm{K}) \quad (4)$$

where the Band II depth ($\mathrm{BII}_{\mathrm{dep}}$) is given in %. From this equation we derived a temperature correction for the Band II depth

$$\Delta\mathrm{BII}_{dep}\ (\%) = 0.015 \times T\ (\mathrm{K}) - 4.5 \quad (5)$$

This correction is derived with respect to the room temperature and must be added to the calculated Band II depth of each asteroid.

An inverse correlation between BAR and temperature was also found for the ordinary chondrites samples. As in the previous cases we obtained an average expression to calculate the rate of change of BAR for a range of temperatures

$$\mathrm{BAR}(T) = 0.83 - 0.00075 \times T\ (\mathrm{K}) \quad (6)$$

from which a temperature correction with respect to room temperature was derived

$$\Delta\mathrm{BAR} = 0.00075 \times T\ (\mathrm{K}) - 0.23 \quad (7)$$

This correction must be added to the calculated BAR values of each asteroid before comparing with those calculated for laboratory samples obtained at room temperature. The temperature corrected Band II depths and BARs are presented in Table 2. Based on the corrected BAR values, the olivine abundance of each asteroid was recalculated using Eq. (1). These values are included in Table 3.

### 2.4. Phase reddening effect on the band parameters

An inspection of the measured Band I depths presented in Table 2 indicates a change of this parameter with phase angle. These values are plotted as a function of phase angle in Fig. 1. The black circles represent the measured Band I depths. Values derived from multiple observations of individual asteroids are connected by lines and have been displayed into two panels for clarity. A tendency of increasing spectral contrast as the phase angle increases is observed for most of the objects in the range of $\sim 2^\circ < g < 70^\circ$. When higher phase angles are included (up to $\sim 90^\circ$) a slight decrease in Band I depth is observed. However, as we do not have sufficient data at such high phase angles, it remains unclear whether this is the actual tendency for $g > 70^\circ$. A similar situation is observed with the temperature corrected Band II depths (Fig. 2). In this case the absorption band seems to increase in the range of $\sim 2^\circ < g < 55^\circ$ and then it remains more or less constant for higher phase angles. In some cases we notice a deviation from these trends among the measured band depths, i.e., a decrease of band depths with increasing phase angle. Although compositional variations cannot be completely ruled out, this is more likely due to the fact that some spectra show more scattering than others, especially in the Band II. This is probably caused by an incomplete correction

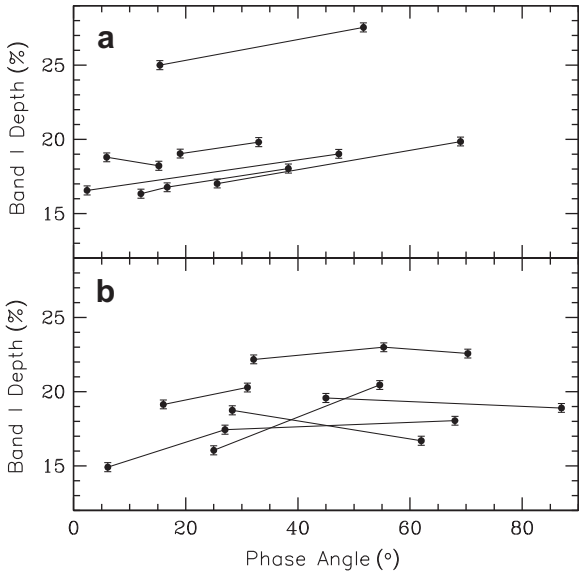


**Fig. 1.** Band I depth as a function of phase angle for the NEAs. Values derived from multiple observations of individual asteroids are connected by lines and have been displayed into two panels for clarity.

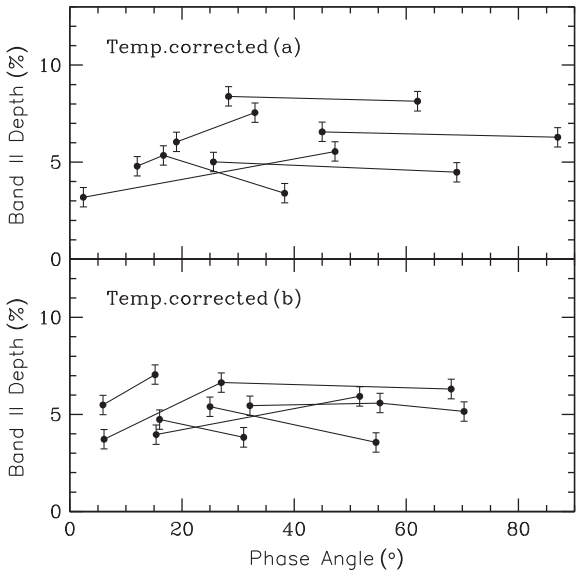


**Fig. 2.** Temperature corrected Band II depth as a function of phase angle for the NEAs. Values derived from multiple observations of individual asteroids are connected by lines and have been displayed into two panels for clarity.

of the telluric water bands, and due to the decreased response of the detector for wavelengths beyond 2.4 μm. This was seen in the Band I of Asteroids 1036 Ganymed ($g = 15.2^\circ$) and 4954 Eric ($g = 62^\circ$) and in the Band II of Asteroids 1620 Geographos ($g = 38.3^\circ$), 1627 Ivar ($g = 31.0^\circ$) and 1980 Tezcatlipoca ($g = 54.6^\circ$).

In an effort to quantify the phase reddening effect on band depths we performed a linear fit to the data of each asteroid. Only the data in the phase angle ranges where the correlations are observed were fitted. Those values that deviate from the general tendency were not consider. The equations derived from the linear fits were then averaged to obtain a general expression for each band depth. Previous works have derived correlations between band parameters and phase angle (e.g., Luu and Jewitt, 1990; Moskovitz et al., 2010). However, these correlations were obtained from mixed observations of different objects, making it very difficult to disentangle the phase reddening from other effects. Our approach, on the other hand, attempts to overcome this problem by evaluating the phase reddening on individual objects from which an average expression is then derived. We caution that this procedure only provides a rough estimation of the effects of phase reddening on band depths, since for each asteroid we have a limited phase angle range. The general equations for the band depths are given by

$$\mathrm{BI}_{dep}(g) = 0.066 \times (g) + 17.42 \quad (8)$$

$$\mathrm{BII}_{dep}(g) = 0.093 \times (g) + 3.73 \quad (9)$$

where the band depths are measured in %. Thus, according to these equations, on average, Band I and Band II depths will increase 0.66% and 0.93% respectively, for every 10° increase in phase angle in the range of $2^\circ < g < 70^\circ$ for Band I and $2^\circ < g < 55^\circ$ for Band II.

From Eqs. (8) and (9) we can obtain expressions for band depth corrections that are a function of the phase angle,

$$\mathrm{BI}_{depc} = \mathrm{BI}_{dep} - 0.066 \times (g) \quad (10)$$

$$\mathrm{BII}_{depc} = \mathrm{BII}_{dep} - 0.093 \times (g) \quad (11)$$

where $\mathrm{BI}_{depc}$ and $\mathrm{BII}_{depc}$ are the corrected band depths. With these equations we can roughly correct the effect of phase reddening in the band depths in the phase angle ranges of $2^\circ < g < 70^\circ$ for Band I and $2^\circ < g < 55^\circ$ for Band II.

The temperature corrected BAR values presented in Table 2 and plotted in Fig. 3 indicate variations with increasing phase angle, however no obvious trend can be seen. The most significant change in BAR is observed for the same objects whose absorption bands show more scattering.

Small variations on band centers with increasing phase angle were found, however they are within the uncertainties associated to these band parameters. This can be seen in Fig. 4 where we plotted Band I center as a function of phase angle for the NEAs. The black circles represent the measured Band I centers. Values derived from multiple observations of the same asteroids are connected by lines.

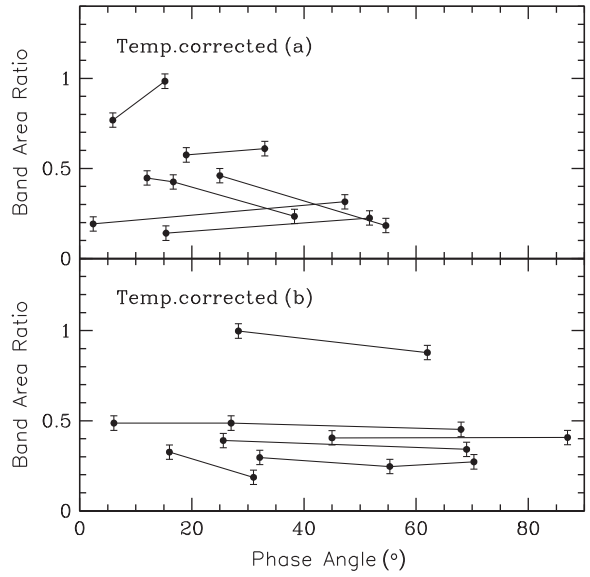


**Fig. 3.** Temperature corrected BAR values as a function of phase angle for the NEAs. Values derived from multiple observations of individual asteroids are connected by lines and have been displayed into two panels for clarity.

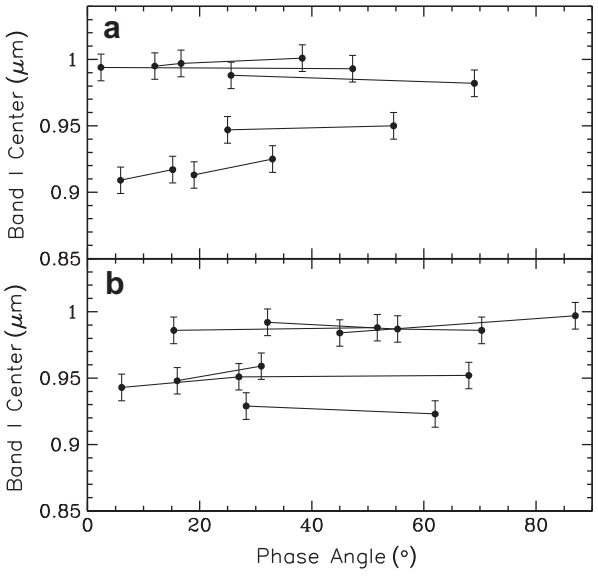


**Fig. 4.** Band I center as a function of phase angle for the NEAs. Values derived from multiple observations of individual asteroids are connected by lines and have been displayed into two panels for clarity.

## 3. Phase reddening from laboratory measurements of ordinary chondrites

### 3.1. Data and spectral band analysis

As it was stated before, ordinary chondrites are considered to be the meteorite analogs of S-complex and Q-type asteroids. Therefore, in order to complement our study we have analyzed the spectra of a group of ordinary chondrites obtained at a wide range of phase angles.

Diffuse reflectance spectra were collected at the University of Winnipeg Planetary Spectrophotometer Facility (UWPSF) using an ASD FieldSpec Pro HR spectrometer over the wavelength range of 0.35–2.5 μm. The three samples that have been analyzed are Dhurmsala (LL6, fell 1860), Pavlograd (L6, fell 1826), and Lancon (H6, fell 1897). They were all crushed and sieved to a grain size of <150 μm. The samples were gently poured into aluminum sample cups and the edge of a glass slide was drawn across the sample to provide a flat surface for the spectral measurements. Reflectance spectra were acquired relative to a 100% Labsphere Spectralon disk measured at an incident angle $i = 13°$ and emission angle $e = 0°$ (13° phase angle). Ten sets of measurements were acquired for each sample resulting in three emission angles ($e = 0°$, 30°, 60°), five incidence angles ($i = 0°$, 13°, 30°, −30°, 60°) and five different phase angles ranging from 13° to 120°. Positive angles ($i$ and $e$) are measured when the light source and the detector are on either side of the normal, while negative incidence angles are measured when both light source and detector are on the same side of the normal. For each measurement, a total of 250 scans were collected and averaged to improve the signal to noise ratio.

Spectral band parameters and their uncertainties were measured for each VIS–NIR spectrum using the same methods applied to the asteroid spectra. In addition to the band parameters we have also measured the spectral slope, which was determined from the fitted continuum across Band I, i.e., a straight line tangent to the reflectance peaks from ∼0.7 to ∼1.55 μm. The uncertainty of the spectral slope is given by the average $1 - \sigma$, estimated from sampling different ranges of points near to the reflectance peaks on either side of the absorption band. The olivine–pyroxene abundance ratio of the samples was estimated using Eq. (1). The band parameters, spectral slopes and $ol/(ol + px)$ ratios with their corresponding errors obtained for each sample are presented in Table 4.

### 3.2. Phase reddening effect on the band parameters

The analysis of the laboratory spectra shows that variations in the band parameters can arise not only by changing the phase angle, but also for the same phase angle using different configurations of the incidence and emission angle. As can be seen in Table 4 phase angles of 30°, 60° and 90° were obtained using different combinations of $i$ and $e$, and these different combinations produced, in some cases, very different band parameter values. Since we want to quantify the effects of phase reddening on the spectral band parameters, for those phase angles where more than one combination of $i$ and $e$ was used the average value for each band parameter was taken. These average values are presented in Table 4.

Fig. 5 shows the reflectance spectra of the LL6 ordinary chondrite at five different phase angles. From the bottom to the top the phase angles are 13°, 30°, 60°, 90° and 120°. The spectra corresponding to $g = 30°$, 60° and 90° are the average spectra obtained from different combinations of the incidence and emission angles. All the spectra are normalized to unity at 0.55 μm. An increase in the spectral slope with increasing phase angle is evident, being more significant for phase angles higher than 30°. A similar

**Table 4**
Spectral band parameters of the ordinary chondrites. The columns in this table correspond to: sample type, the incidence angle ($i$), the emission angle ($e$), the phase angle ($g$), the spectral slope ±0.004, the Band I center (BI ± 0.003), the Band I depth ($BI_{dep}$ ± 0.1), the Band II center (BII ± 0.005), the Band II depth ($BII_{dep}$ ± 0.2), the band area ratio (BAR ± 0.01) and the olivine–pyroxene abundance ratio ($ol/(ol + px)$ ± 0.03).

| Sample | $i$ (°) | $e$ (°) | $g$ (°) | Slope (%μ$^{-1}$) | BI (μm) | $BI_{dep}$ (%) | BII (μm) | $BII_{dep}$ (%) | BAR | $ol/(ol + px)$ |
|---|---|---|---|---|---|---|---|---|---|---|
| LL6 | 13 | 0 | 13 | −0.127 | 0.984 | 36.81 | 1.963 | 17.27 | 0.58 | 0.59 |
| LL6 | 30 | 0 | 30 | −0.094 | 0.982 | 38.41 | 1.959 | 18.35 | 0.58 | 0.59 |
| LL6 | 0 | 30 | 30 | −0.083 | 0.978 | 38.47 | 1.961 | 18.73 | 0.61 | 0.58 |
| LL6 | −30 | 60 | 30 | −0.179 | 0.978 | 36.69 | 1.964 | 18.36 | 0.63 | 0.58 |
| LL6 | 30,0,−30 | 0,30,60 | 30 | −0.119 | 0.979 | 37.86 | 1.961 | 18.48 | 0.61 | 0.58 |
| LL6 | 60 | 0 | 60 | 0.002 | 0.981 | 40.28 | 1.957 | 18.55 | 0.55 | 0.59 |
| LL6 | 0 | 60 | 60 | −0.097 | 0.969 | 37.30 | 1.965 | 18.89 | 0.68 | 0.56 |
| LL6 | 30 | 30 | 60 | −0.043 | 0.982 | 39.61 | 1.960 | 18.22 | 0.56 | 0.59 |
| LL6 | 60,0,30 | 0,60,30 | 60 | −0.046 | 0.977 | 39.06 | 1.961 | 18.55 | 0.60 | 0.58 |
| LL6 | 60 | 30 | 90 | 0.099 | 0.973 | 37.91 | 1.963 | 18.75 | 0.62 | 0.58 |
| LL6 | 30 | 60 | 90 | 0.184 | 0.980 | 36.84 | 1.961 | 16.46 | 0.53 | 0.60 |
| LL6 | 60,30 | 30,60 | 90 | 0.141 | 0.976 | 37.38 | 1.962 | 17.61 | 0.57 | 0.59 |
| LL6 | 60 | 60 | 120 | 0.212 | 0.972 | 34.18 | 1.959 | 17.50 | 0.67 | 0.57 |
| L6 | 13 | 0 | 13 | −0.102 | 0.949 | 42.37 | 1.944 | 18.70 | 0.57 | 0.59 |
| L6 | 30 | 0 | 30 | −0.090 | 0.951 | 42.71 | 1.943 | 18.92 | 0.56 | 0.59 |
| L6 | 0 | 30 | 30 | −0.089 | 0.950 | 42.39 | 1.945 | 19.03 | 0.58 | 0.59 |
| L6 | −30 | 60 | 30 | −0.192 | 0.950 | 41.58 | 1.947 | 18.00 | 0.57 | 0.59 |
| L6 | 30,0,−30 | 0,30,60 | 30 | −0.124 | 0.951 | 42.23 | 1.945 | 18.65 | 0.57 | 0.59 |
| L6 | 60 | 0 | 60 | −0.084 | 0.954 | 43.16 | 1.945 | 18.21 | 0.51 | 0.60 |
| L6 | 0 | 60 | 60 | −0.085 | 0.949 | 43.36 | 1.948 | 18.73 | 0.59 | 0.59 |
| L6 | 30 | 30 | 60 | 0.004 | 0.947 | 44.68 | 1.939 | 20.86 | 0.62 | 0.58 |
| L6 | 60,0,30 | 0,60,30 | 60 | −0.055 | 0.950 | 43.73 | 1.944 | 19.26 | 0.57 | 0.59 |
| L6 | 60 | 30 | 90 | 0.097 | 0.945 | 42.53 | 1.941 | 17.21 | 0.51 | 0.61 |
| L6 | 30 | 60 | 90 | 0.177 | 0.944 | 41.69 | 1.948 | 17.24 | 0.56 | 0.59 |
| L6 | 60,30 | 30,60 | 90 | 0.137 | 0.944 | 42.11 | 1.945 | 17.23 | 0.54 | 0.60 |
| L6 | 60 | 60 | 120 | 0.191 | 0.944 | 39.84 | 1.943 | 16.15 | 0.51 | 0.61 |
| H6 | 13 | 0 | 13 | −0.141 | 0.934 | 35.45 | 1.930 | 18.41 | 0.88 | 0.52 |
| H6 | 30 | 0 | 30 | −0.151 | 0.935 | 36.20 | 1.929 | 19.12 | 0.89 | 0.51 |
| H6 | 0 | 30 | 30 | −0.115 | 0.933 | 35.33 | 1.934 | 18.33 | 0.88 | 0.52 |
| H6 | −30 | 60 | 30 | −0.177 | 0.931 | 34.80 | 1.931 | 18.26 | 0.93 | 0.50 |
| H6 | 30,0,−30 | 0,30,60 | 30 | −0.148 | 0.933 | 35.44 | 1.932 | 18.57 | 0.90 | 0.51 |
| H6 | 60 | 0 | 60 | −0.149 | 0.935 | 36.48 | 1.926 | 18.91 | 0.83 | 0.53 |
| H6 | 0 | 60 | 60 | −0.096 | 0.929 | 34.54 | 1.935 | 16.93 | 0.84 | 0.52 |
| H6 | 30 | 30 | 60 | −0.096 | 0.933 | 36.93 | 1.931 | 17.85 | 0.76 | 0.55 |
| H6 | 60,0,30 | 0,60,30 | 60 | −0.114 | 0.933 | 35.98 | 1.931 | 17.90 | 0.81 | 0.53 |
| H6 | 60 | 30 | 90 | −0.058 | 0.932 | 34.77 | 1.928 | 17.65 | 0.83 | 0.53 |
| H6 | 30 | 60 | 90 | −0.012 | 0.926 | 31.69 | 1.934 | 14.77 | 0.84 | 0.53 |
| H6 | 60,30 | 30,60 | 90 | −0.035 | 0.929 | 33.23 | 1.931 | 16.21 | 0.83 | 0.53 |
| H6 | 60 | 60 | 120 | 0.020 | 0.932 | 31.77 | 1.932 | 15.55 | 0.80 | 0.54 |

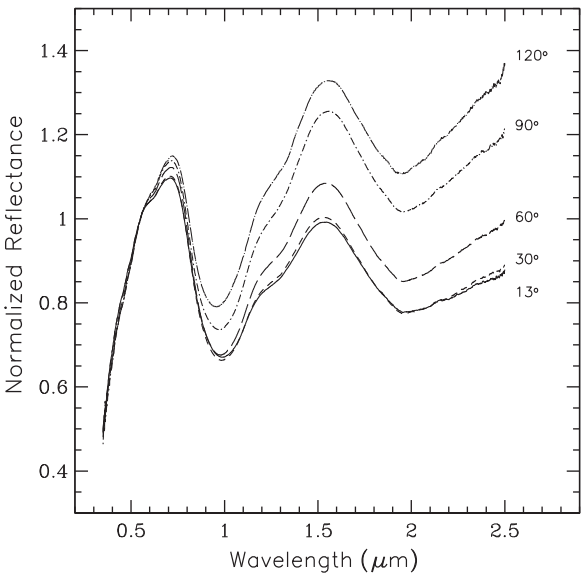


**Fig. 5.** Reflectance spectra of the LL6 chondrite Dhurmsala obtained at five different phase angles. From the bottom to the top $g = 13°$ (solid line), $g = 30°$ (short dashed line), $g = 60°$ (long dashed line), $g = 90°$ (dot-short dashed line) and $g = 120°$ (dot-long dashed line). All the spectra are normalized to unity at 0.55 μm.

behavior was observed for the other two samples. For phase angles between 13° and 30° a slight reddening is observed in the LL6 spectra, while a slight blueing (i.e decreasing of the spectral slope with increasing phase angle) is seen in the L6 and H6 spectra. Variations in the strengths of the absorption bands are also seen for the three samples.

In Fig. 6 we plotted the spectral slopes (panel a), the BAR values (panel b), the Band I depths (panel c), the Band II depths (panel d) and the band centers (panels e and f) as functions of the phase angle for the LL6 ordinary chondrite. The dashed lines are polynomial fits.

From the "a" panel we can see that the measured spectral slopes remain more or less constant for phase angles between 13° and 30°, and then they increase as the phase angle increases up to 120°. A similar trend was observed for the L6 and H6 ordinary chondrites. The largest difference in spectral slope between the lowest (13°) and the highest (120°) phase angle was found for the LL6 ordinary chondrite, which increased 0.34%μ$^{-1}$, followed by the L6 ordinary chondrite with an increase of 0.29%μ$^{-1}$ and the H6 ordinary chondrite with an increase of 0.16%μ$^{-1}$.

The Band I depth of the three samples has its maximum spectral contrast near $g = 60°$. The LL6 spectra show a progressive increase of Band I depth from $g = 13°$ to 60° (Fig. 6 panel c), however the L6 and H6 spectra show almost no change in Band I depth for phase angles between 13° and 30°, and then an increase in Band I depth

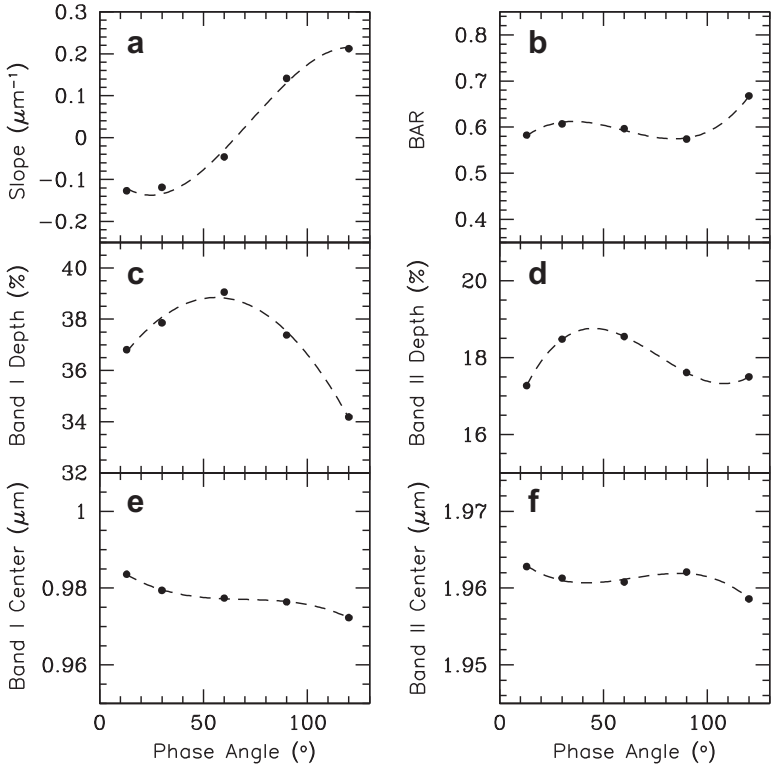


**Fig. 6.** LL6 ordinary chondrite: Measured spectral slopes (a), BAR values (b), Band I depths (c), Band II depths (d) Band I centers (e) and Band II centers (f) as a function of the phase angle. The error bars are smaller than the symbols. The dashed lines represent polynomial fits.

from $g = 30°$ to 60°. The spectra of the three samples show a decrease in Band I depth between 60° and 120° phase angle. The largest increase in Band I depth between the lowest phase angle (13°) and the phase angle at which the Band I reaches its maximum spectral contrast (~60°) corresponds to the LL6 sample, with an increase of 2.25%, followed by the L6 and H6 with an increase of 1.36 and 0.53% respectively. Of the three samples, the LL6 also shows the most significant decrease of Band I depth between the phase angle corresponding to the maximum spectral contrast and the highest phase angle (120°), with a decrease of 4.88%, followed by the H6 with a decrease of 4.21% and the L6 with a decrease of 3.89%.

The behavior of the Band II depths seems to be more complex. The LL6 spectra show a progressive increase of Band II depths from $g = 13°$ to ~45° (where the band reaches its maximum spectral contrast) and then it drops between 45° and 90°, becoming more or less constant from 90° to 120° phase angle (Fig. 6 panel d). The Band II depths of the L6 spectra show almost no change between 13° and 30°. From 30° to 60° Band II depths increase and beyond 60° gradually decrease with phase angle increasing to 120°. The Band II depths of the H6 spectra show a slight increase from 13° to 30° and then drop from 30° to 120°. The most significant increase in Band II depths between the lowest phase angle and the phase angle at which the Band II reaches its maximum spectral contrast was observed for the LL6 sample, which shows an increase of 1.56%, followed by the L6 with an increase in Band II depth of 0.56% and the H6 with the lowest increase of 0.16%. The largest difference in Band II depth between the phase angle corresponding to the maximum spectral contrast and the largest phase angle (120°) was observed for the L6 sample that shows a decrease of 3.11%, followed by the H6 with a decrease of 3.02% and the L6 with a decrease of 1.33%.

Variations in the BAR values are observed among the three samples, being the maximum difference between the lowest and highest phase angle ~0.1, however no systematic trends were found. A similar situation occur with the band centers, where the maximum shift (to shorter wavelengths) between the lowest and highest phase angle is ~0.01 μm for the Band I center of the LL6 sample (Fig. 6 panel e).

## 4. Phase reddening and mineralogical analysis

The analysis of the laboratory samples indicate that the (olivine-rich) LL6 ordinary chondrite is the most affected by phase reddening. This sample shows the largest variation in spectral slopes and band depths with increasing phase angles. This material-dependence of the phase reddening confirm the results reported by previous studies (e.g., Adams and Filice, 1967; Gradie et al., 1980). A comparison between the measurements obtained from the laboratory samples with those from the NEAs spectra, reveal that the rate of change in band depths for the ordinary chondrites is lower than that found for the asteroids. Differences in grain size, composition and packing between the NEAs studied and the meteorite samples could explain this discrepancy. Of the three samples, the spectral behavior of the LL6 is the closest to the NEAs. This resemblance could be attributed to the fact that half of the asteroids studied are located in the same region as the LL ordinary chondrites in the Band I center versus BAR diagram (see Figs. 10 and 11).

Because band centers and composition of mafic minerals are related, these band parameters are used to derive information about the pyroxene and olivine composition of asteroids surfaces. For that purpose, and from the analysis of laboratory samples, different empirical equations have been derived (e.g., Gaffey et al., 2002; Burbine et al., 2007; Dunn et al., 2010). Our results show that there is no significant change in band centers with increasing phase angle for both asteroid and meteorite spectra, being the largest shift

of ~0.01 μm (for the meteorite spectra), which is on the order of the uncertainty associated with this parameter for the asteroid spectra. Based on this, it seems to be unlikely that phase reddening could lead to a misinterpretation of the minerals composition in asteroids.

In addition to the band centers, we used the BAR values and Eq. (1) to estimate olivine and pyroxene abundances for both NEAs and the laboratory samples. The results obtained (Tables 3 and 4) show that the largest variation in the $ol/(ol+px)$ ratio with increasing phase angles for NEAs is ~0.02 (not taken into account the values obtained from the noisy spectra), and for the ordinary chondrites between 0.03 and 0.05. Since these variations are on the order of the errors, effects of phase reddening on the estimation of the olivine–pyroxene abundance ratio seems to be negligible.

## 5. Phase reddening and space weathering

Space weathering is the term commonly used to refer to any process that modifies the surfaces of airless bodies. The effects of space weathering on the spectra can be seen as reddening of the spectral slopes and suppression of the absorption bands, (Pieters et al., 2000; Hapke, 2001; Gaffey, 2010). The analysis of returned samples from the Moon and Asteroid (25143) Itokawa have shown that the cause of the spectral changes is the presence of submicroscopic metallic iron (SMFe) incorporated into the soil grains (Pieters et al., 2000; Taylor et al., 2001; Noguchi et al., 2011). This SMFe is produced by condensation of vapors created by micrometeorite impacts and/or deposition of atoms sputtered off from silicates by solar wind ions (Taylor et al., 2001; Hapke, 2001; Clark et al., 2002a). Ion irradiation experiments conducted by Brunetto and Strazzulla (2005) showed that solar wind irradiation can also redden reflectance spectra by creation of displacements (the sum of the vacancies and the replacements) caused by elastic collisions between ions and target nuclei.

Brunetto et al. (2006) determined that the effects of space weathering due to ion irradiation can be described by an exponential continuum. They computed the ratio between the reflectance spectra of irradiated and unirradiated samples and then modeled it with an exponential curve given by

$$\text{Ratio} = W(\lambda) = K\exp(C_S/\lambda) \tag{12}$$

where $\lambda$ is the wavelength, $K$ is a scale factor and the parameter $C_S$ is a measure of the effects of space weathering. They called $W(\lambda)$ the weathering function. Since both effects, phase reddening and space weathering, are manifested in a similar way, we investigated whether the red slopes exhibited by spectra obtained at high phase angles could be misinterpreted as space weathering. In order to do this we carried out two different experiments.

For the first experiment we followed the same procedure used by Brunetto et al. (2006), with the difference that instead of dividing the reflectance spectra of an irradiated by an unirradiated sample, we computed the ratio between the spectra obtained at high phase angles and those obtained at low phase angles. Since there is no significant change in spectral slope between $g = 13°$ and 30° we used the spectrum obtained at a phase angle of 30° as reference point. Fig. 7 shows the ratio plots (solid lines) between the spectra of the LL6 obtained at $g = 60°$ and $g = 30°$ (bottom), at $g = 90°$ and $g = 30°$ (middle) and at $g = 120°$ and $g = 30°$ (top panel). The ratio plots were modeled by fitting the same exponential curve used by Brunetto et al. (2006)

$$\text{Ratio} = P_R(\lambda) = A\exp(C_P/\lambda) \tag{13}$$

where we have just changed the name of the function, we call it the phase reddening function ($P_R$) and the parameters $A$ and $C_P$ are equivalents to the parameters $K$ and $C_S$ respectively, with the difference that $C_P$ would be a measure of the effect of the phase reddening. The best fit curves obtained using Eq. (13) are represented with dashed lines in Fig. 7. Here we have used the LL6 spectra as an example, but the same procedure can be used with the other samples. In Fig. 7 we have also included the resultant $A$ and $C_P$ values and the coefficient of determination ($R^2$) of the fitted curves for each ratio plot. Similarly to the results obtained by Brunetto et al. (2006) the ratio of the spectra show some traces of Bands I and II, which can affect the fitting in those spectral regions. Nevertheless, the $R^2$ for the fitted curves ranges between 0.88 and 0.96 and, in general, the results are comparable to those of Brunetto et al. (2006). After comparing the $C_P$ values with the $C_S$ obtained by Brunetto et al. (2006) for different samples, we found that the $C_P$ values are similar to the $C_S$ obtained for the H5 ordinary chondrite Epinal, which was irradiated with $Ar^{++}$ (60 keV) at three different ion fluences.

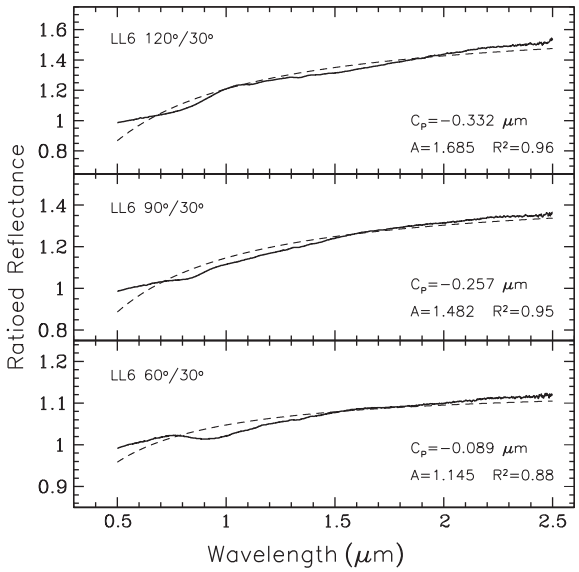


**Fig. 7.** Ratio plots (solid lines) between the spectra of the LL6 obtained at $g = 60°$ and $g = 30°$ (bottom), at $g = 90°$ and $g = 30°$ (middle) and at $g = 120°$ and $g = 30°$ (top panel). Dashed curves are the best fit curves obtained using Eq. (13). For each ratio plot the resultant A, $C_P$ and $R^2$ values are given.

Brunetto et al. (2006) found that there is a strong correlation between the $C_S$ parameter and the number of displacements per $cm^2$ (damage parameter). From their experimental data they were able to create a damage curve that was fitted by

$$C_S = \alpha\ln(\beta d + 1) \tag{14}$$

where $d$ is the damage parameter, $\alpha = -0.33 \pm 0.06$ μm and $\beta = (1.1 \pm 0.5) \times 10^{-19}$ $cm^2$. Using this equation we calculated the number of displacements per $cm^2$ that would correspond to our $C_P$ values. It is important to point out that in this case the $d$ values calculated using the $C_P$ have no real physical meaning, since the $C_P$ parameter quantifies the effect of the phase reddening and not the space weathering, however their calculation is useful to illustrate how the phase reddening can resemble different degrees of space weathering. This can be seen in Fig. 8 where we have plotted the $C_P$ (LL6 ordinary chondrite) and $C_S$ (Epinal ordinary chondrite) values versus the calculated damage parameter for each sample. The LL6 data are represented with filled symbols while the Epinal values are plotted as open symbols. These results indicate that an increase in phase angle in the range of 30–120° would be equivalent to irradiate the sample with high mass ions ($Ar^{++}$ 60 keV) with an ion fluence in the range of $\sim 1.3 \times 10^{15}$–$1.7 \times 10^{16}$ ions $cm^{-2}$. These ion fluences are equivalent to exposure times of $\sim 0.1 \times 10^6$–$1.3 \times 10^6$ years at about 1 AU from the Sun (calculated as in

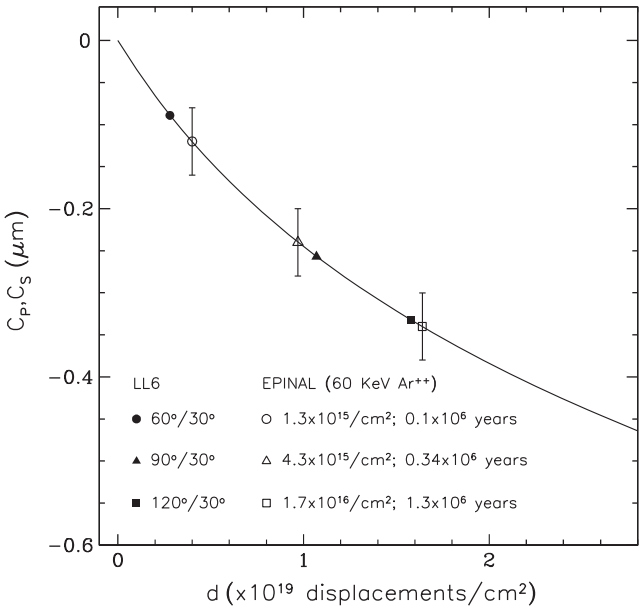


**Fig. 8.** The $C_P$ (LL6 ordinary chondrite) and $C_S$ (Epinal ordinary chondrite) parameters as a function of the number of displacements per cm$^2$ (damage parameter). The data corresponding to the Epinal meteorite were obtained from Brunetto et al. (2006). The LL6 and the Epinal data are plotted as filled and open symbols respectively. For the LL6 each symbol represents the value obtained from the ratioed spectra of different phase angles. The symbols corresponding to the Epinal meteorite represent different ions fluences. Approximate exposure times (at 1 AU) corresponding to each ion fluence are also shown. The solid line represents the experimental damage curve from Brunetto et al. (2006). The error bars of the LL6 data are on the order of the size of symbols.

Strazzulla et al. (2005)). Laboratory experiments (e.g., Strazzulla et al., 2005) have shown that the timescale for the weathering of NEAs surfaces due to ion irradiation is on the order of $10^4$–$10^6$ years. Thus, observing NEAs at high phase angles could produce spectral slopes that resemble those exhibited by weathered surfaces.

For the second experiment we modeled the optical effects of the SMFe on the laboratory spectra by using Hapke's radiative transfer model (Hapke, 1981, 1993, 2001), and then we compared these spectra with those obtained at different phase angles.

From Hapke (2001) the bidirectional reflectance of a medium of isotropic scatterers ignoring the opposition effect is given by

$$r(i,e,g) = \frac{w}{4\pi}\frac{\mu_0}{\mu_0+\mu}H(\gamma,\mu_0)H(\gamma,\mu) \tag{15}$$

where $i$, $e$ and $g$ are the incidence, emission and phase angle respectively, $\mu_0 = \cos(i)$, $\mu = \cos(e)$, $w$ is the single scattering albedo, $\gamma = (1-w)^{1/2}$, and $H(\gamma,\mu)$ is an analytic approximation to the Ambartsumian–Chandrasekhar H functions. Since most reflectances are relative to a standard, Hapke (2001) represented this relative reflectance as

$$\Gamma(\gamma) = \frac{1-\gamma^2}{(1+2\gamma\mu_0)(1+2\gamma\mu)} \tag{16}$$

from which $\gamma$ can be determined, and the single scattering albedo of the sample can be calculated as

$$w = 1-\gamma^2 \tag{17}$$

The single scattering albedo can be also written as a function of the properties of the particles of the medium by

$$w = S_e + (1-S_e)\frac{1-S_i}{1-S_i\Theta}\Theta \tag{18}$$

where $S_e$ is the Fresnel reflection coefficient for externally incident light, $S_i$ is the Fresnel reflection coefficient for internally scattered light (see Hapke, 2001), and $\Theta$ is the single-pass transmission of the particle. If there is no internal scattering, then

$$\Theta = e^{-\alpha\langle D\rangle} \tag{19}$$

where $\langle D\rangle$ is the mean ray path length (Hapke, 1993) and $\alpha$ is the absorption coefficient given by

$$\alpha = \frac{4\pi nk}{\lambda} \tag{20}$$

where $n$ and $k$ are the real and imaginary part of the refractive index respectively and $\lambda$ is the wavelength. From Eqs. (18) and (19) the absorption coefficient can be also calculated as

$$\alpha = \frac{1}{\langle D\rangle}\ln\left[S_i + \frac{(1-S_e)(1-S_i)}{w-S_e}\right] \tag{21}$$

To model the effects of the SMFe, the absorption coefficient of the host material ($\alpha_h$) is increased by adding to it the absorption coefficient of the SMFe ($\alpha_{Fe}$). Using the Maxwell–Garnett effective medium theory, Hapke (2001) derived an expression to calculate $\alpha_{Fe}$,

$$\alpha_{Fe} = \frac{36\pi z f \rho_h}{\lambda\rho_{Fe}} \tag{22}$$

where $f$ is the mass fraction of the Fe particles, $\rho_h$ is the density of the host material, $\rho_{Fe}$ is the density of iron and $z$ is given by

$$z = \frac{n_h^3 n_{Fe}k_{Fe}}{\left(n_{Fe}^2 - k_{Fe}^2 + 2n_h^2\right)^2 + (2n_{Fe}k_{Fe})^2} \tag{23}$$

where $n_h$ and $n_{Fe}$ are the real part of the refractive indices of the host material and iron respectively, and $k_{Fe}$ is the imaginary part of the refractive index of iron. Thus, if we use Eq. (21) to calculate the absorption coefficient of the host material ($\alpha_h$), then the absorption coefficient of the material containing SMFe is given by

$$\alpha_w = \alpha_h + \alpha_{Fe} \tag{24}$$

Looking at Eqs. (15) and (18)–(20) we can understand why phase reddening and space weathering are manifested in similar ways. Reflectance spectra are controlled by the single scattering albedo ($w$), which is a function of the absorption coefficient ($\alpha$). The absorption coefficient is a parameter that characterizes how deep into a material light of a particular wavelength can penetrate before being absorbed. As the phase angle increases, light is less able to escape from the medium, meaning that photons are more absorbed, resulting in a decrease of reflectance throughout the entire spectrum. However, because the absorption coefficient is inversely proportional to the wavelength (the shorter the wavelength the higher the absorption coefficient) the reflectance in the blue part of the spectrum will decrease faster than in the red part, producing the increase in spectral slope (reddening). Similarly, the addition of the SMFe (Eq. (24)) will decrease the blue part of the spectrum more than the red part due to the stronger absorption at short wavelengths, increasing the spectral slope (Hapke, 2001).

For our experiment we used the spectrum of the LL6 ordinary chondrite obtained at a phase angle of 13° as reference point. Using these data we first calculated $\alpha_h$ with Eqs. (16)–(21), where we have assumed $n_h = 1.7$, which is a typical value for mafic minerals (Hapke, 2001). Then using Eqs. (22) and (23) we estimated $\alpha_{Fe}$. For this calculation we have assumed $\rho_h = 3.48$, which is the average grain density for LL chondrites (Britt and Consolmagno, 2003) and $\rho_{Fe} = 7.87$. The optical constants of iron, $n_{Fe}$ and $k_{Fe}$, were taken from Johnson and Christy (1974). Since these values were measured only for $\lambda \sim 1.9$ μm, we did a polynomial fit to the data in order to extrapolate them to 2.5 μm. The $\alpha_{Fe}$ was calculated for different mass fractions of Fe and then the resulting values were

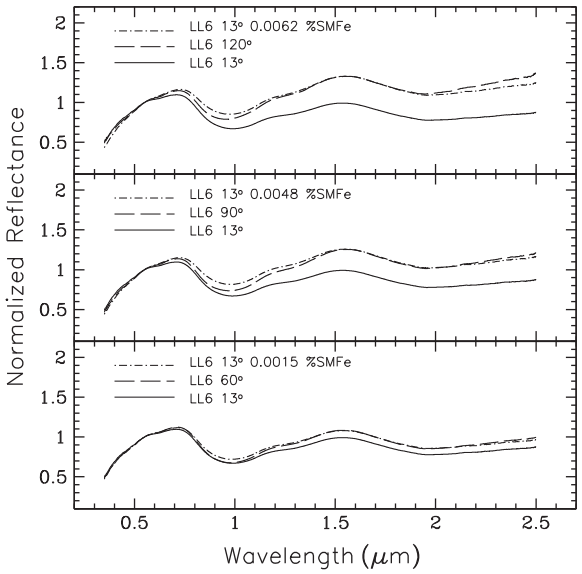


**Fig. 9.** Reflectance spectra of the LL6 chondrite Dhurmsala after adding different amounts of SMFe (dot-short dashed lines) to the spectrum obtained at $g = 13°$. For comparison the spectra of the LL6 obtained at $g = 13°$ (solid lines) and $g = 60°$, 90° and 120° (long dashed lines from the bottom to the top) have been included. All the spectra are normalized to unity at 0.55 μm.

added to the calculated $\alpha_h$ in order to obtain $\alpha_w$. These $\alpha_w$ values were then inserted into Eq. (19), which combined with Eq. (18) allowed us to determine the new single scattering albedos. Finally, we calculated $\gamma$ from Eq. (17) and using Eq. (16) we obtained the "weathered spectra" for the different % of SMFe. In Fig. 9 we plot the reflectance spectra of the LL6 after adding different amounts of SMFe. We found that the spectrum obtained at $g = 60°$ shows a spectral slope comparable to the spectrum obtained at $g = 13°$ after adding 0.0015% SMFe. For phase angles of 90° and 120° the spectral slopes are equivalent to adding 0.0048 and 0.0062% SMFe respectively, to the spectrum obtained at $g = 13°$. If we consider that an amount of ~0.02% of SMFe is required to explain the red slopes of some S-complex asteroids (e.g., Hapke, 2001; Rivkin et al., 2004), this means that the spectral slope for the highest phase angle ($g = 120°$) would be equivalent to ~30% of that SMFe.

## 6. Phase reddening and taxonomic classification

The taxonomic classification of asteroids is based on shared observational parameters like spectral slope, color, albedo and band depth. Most of the current classification systems are based on visible data (e.g., Tholen, 1984; Bus and Binzel, 2002b,a), in part because only during the last decade sufficient high-quality NIR spectral data became available to extend the classification to the near-infrared wavelengths. Two of the most common systems used to classify asteroids using VIS–NIR data are those introduced by Gaffey et al. (1993) and more recently by DeMeo et al. (2009). Gaffey et al. (1993) developed their classification system from the analysis of 39 asteroids classified as S-type by Tholen (1984). They divided the S-population into seven main compositional subgroups designated S(I)–S(VII). These subgroups range from pure olivine through olivine–pyroxene mixtures to pure pyroxene mixtures, and were derived on the basis of two band parameters, the Band I center and the BAR. The Bus–DeMeo taxonomy, on the other hand, is based on Principal Component Analysis and is comprised of 24 classes that include three major complexes (S-, C- and X-complex) and the end members O, Q, R, V, D, K, L, T. The S-complex is subdivided into S, Sa, Sq, Sr and Sv. Since both taxonomic systems use band depths as one of the primary criteria to classify the objects, multiple observations of the same asteroid obtained at different phase angles could lead to ambiguous classifications. In order to test the influence of phase reddening on the taxonomic classification, we have applied the two classification systems described above to each of the observed asteroids.

Fig. 10 shows the measured Band I center versus BAR for the NEAs. Within the uncertainties all the NEAs studied are classified either as S(III) or S(IV). There are four cases (1620 Geographos, 1627 Ivar, 1980 Tezcatlipoca and 1036 Ganymed) that show large variations of the BAR from one phase angle to another, but this is likely attributed to noisy spectra rather than phase reddening. The rest of the asteroids show variations in Band I centers and BAR that are on the order of the error bars. The results obtained from the laboratory samples (Fig. 11) indicate that the largest variation in the BAR (~0.1) is larger than the typical uncertainty associated with the BAR values measured from asteroids (represented by the $1-\sigma$ error bars in the upper corner of this figure). This means that in certain cases phase reddening could contribute to an ambiguous classification, particularly if the measured band parameters of the object are located close to the boundaries that define each class.

The classification into the Bus–DeMeo system was done using the online taxonomy calculator (http://smass.mit.edu/busdemeoclass.html). The class assigned to each spectrum and the calculated principal components PC1′ and PC2′ are given in Table 3. Only in three cases asteroids were ambiguously classified. Asteroid (1036) Ganymed was classified as S and Sr, (1620) Geographos was classified as S and Sq and (4954) Eric was classified as Sw and Sr. The letter "w" was introduced by DeMeo et al. (2009) to indicate an object exhibiting a high slope, but does not represent a different class, thus an object designated as "Sw" is an asteroid

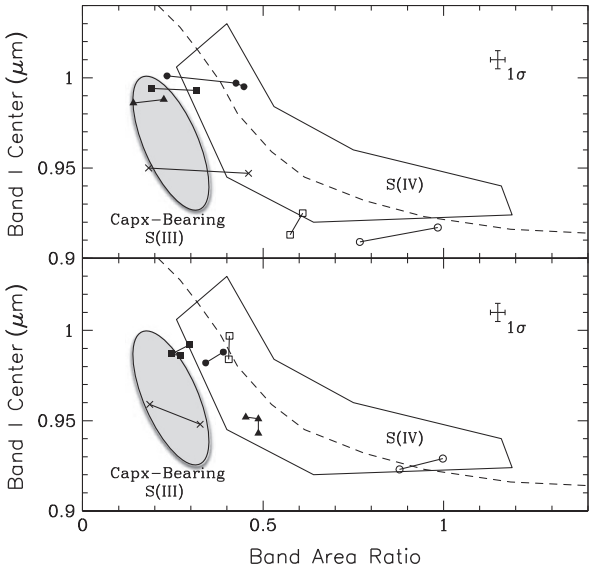


**Fig. 10.** Plot of the Band I center versus BAR for the NEAs. The polygonal region represents the mafic silicate components of ordinary chondrites and S(IV) asteroids (Gaffey et al., 1993). The gray oval region represents the mineralogical zone corresponding to the calcic pyroxene-bearing where the S(III) subtypes are located (Gaffey et al., 1993). The dashed curve indicates the location of the olivine–orthopyroxene mixing line (Cloutis et al., 1986). The top panel shows the measured values for Asteroids 1620 Geographos (filled circles), 1036 Ganymed (open circles), 1862 Apollo (filled triangles), 1980 Tezcatiploca (crosses), 11398 (open squares) and 6239 Minos (filled squares). The bottom panel shows the measured values for Asteroids 4954 Eric (open circles), 66146 (filled squares), 1627 Ivar (crosses), 35107 (open squares), 25143 Itokawa (filled circles) and 4179 Toutatis (filled triangles). Measured values from multiple observations of individual asteroids are connected by lines. The average $1-\sigma$ error bars are shown in the upper right corner.

classified as S-type that exhibit a higher slope than the typical S-types. This distinction is based on an arbitrary cutoff at slope = 0.25 (DeMeo et al., 2009). Table 3 shows that the notation of "w" was added to many asteroids from one phase angle to another. Certainly the phase reddening most play a role on this variation in spectral slope, however as it was stated earlier this is a very sensitive parameter that can be affected by other factors. What is important to point out is that in the Bus–DeMeo system the spectral slope is removed prior to the classification. For those objects which were given two classifications it is likely that the phase reddening was not the only contribution, since some of the spectra show more scatter than others. However from our analysis we estimate an average variation of about 0.04 and 0.03 for the PC1′ and PC2′ respectively, that could be attributed to phase reddening. These results suggest that phase reddening could lead to an ambiguous classification but only if the calculated PC values are close to the lines that separate each class. This can be seen in Fig. 12 where we have plotted the PC values in a PC1′ versus PC2′ diagram from DeMeo et al. (2009). For clarity only the calculated PC values for some of the asteroids have been plotted. These values are represented by different symbols, which are connected by lines to indicate multiple values for individual asteroids.

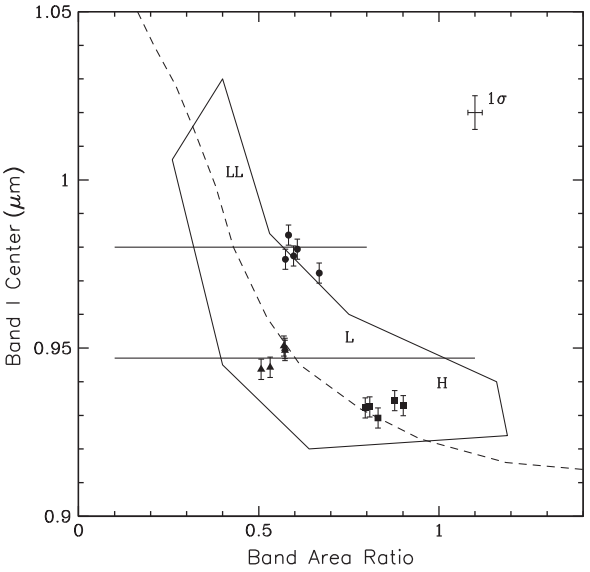


**Fig. 11.** Plot of the Band I center versus BAR for the LL6 (circles), L6 (triangles) and H6 (squares) ordinary chondrites. The polygonal region represents the mafic silicate components of ordinary chondrites and S(IV) asteroids (Gaffey et al., 1993). The dashed curve indicates the location of the olivine–orthopyroxene mixing line (Cloutis et al., 1986). The horizontal lines represent the approximate boundaries that separate the three types of ordinary chondrites found by Dunn et al. (2010). The error bar in the *x*-axis is of the order of the size of symbols. For comparison purpose we have included the average $1-\sigma$ error bars (upper right corner) associated with the Band I center and BAR value measured for asteroids.

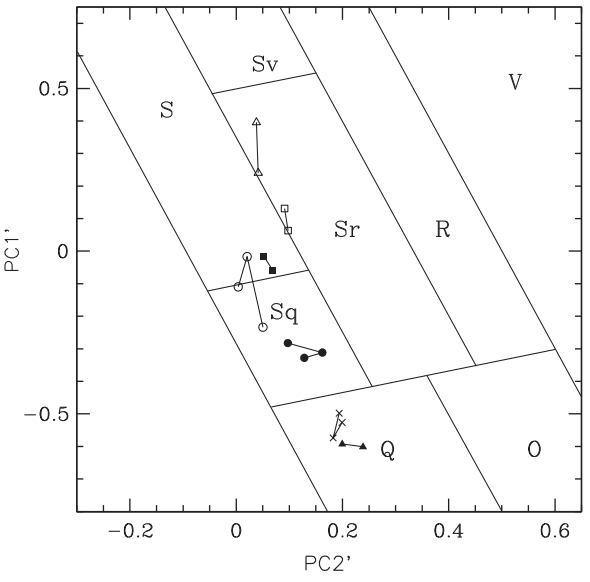


**Fig. 12.** Calculated PC values for some of the NEAs studied represented in a PC1′ versus PC2′ diagram from DeMeo et al. (2009). The letters indicate the different classes within the S-complex plus Q-, O-, R- and V-types. The asteroids whose calculated PC values have been plotted are: (1036) Ganymed (open triangles), (1620) Geographos (open circles), (1627) Ivar (filled squares), (4179) Toutatis (filled circles), (1862) Apollo (filled triangles), 11398 (open squares) and 66146 (crosses).

## 7. Conclusions

The analysis of VIS–NIR spectra of 12 NEAs observed at different phase angles has revealed an increase of band depths with increasing phase angles in the range of $2^\circ < g < 70^\circ$ for Band I and $2^\circ < g < 55^\circ$ for Band II. Our analysis showed that, on average, Band I and Band II depths will increase 0.66% and 0.93% respectively, for every 10° increase in phase angle. From the available data we have derived equations that can be used to correct the effects of phase reddening in the band depths. Small variations in band centers and BAR values with increasing phase angle were also found. Similar trends were observed in the laboratory spectra of three different types of ordinary chondrites. In addition, an increase in the spectral slope with increasing phase angles was found for the ordinary chondrites. This increase in spectral slope is more significant for phase angles higher than 30°. Of the three types of ordinary chondrites the (olivine-rich) LL6 is the most affected by phase reddening, showing the largest variations in spectral slopes and band depths with increasing phase angles. These variations in spectral band parameters seems to have no significant impact on the mineralogical analysis though. We have also found that the increase in spectral slope caused by phase reddening can mimic the effect of space weathering. In particular, an increase in phase angle in the range of 30–120° will produce a reddening of the reflectance spectra equivalent to exposure times of $\sim 0.1 \times 10^6$–$1.3 \times 10^6$ years at about 1 AU from the Sun. Furthermore, the increase in spectral slope due to phase reddening is comparable to the effects caused by the addition of various amounts of SMFe. These results imply that phase reddening should be considered when studying space weathering effects on spectral data. Regarding to the taxonomic classification, we found that phase reddening can lead to an ambiguous classification, but only if the measured spectral band parameters and/or principal components (depending on the taxonomic system) are located close to the boundaries that define each class.

## Acknowledgments

The authors thank, Francesca DeMeo, John Hinrichs and Paul Lucey for providing us with data for this research. We also thank to Michael Gaffey for the meteorite samples and Stefan Schröder and Silvia Protopapa for the fruitful discussions related to this work. We would also like to thank Tasha Dunn and Jian-Yang Li for their reviews, which helped to improve the manuscript. J.A. Sanchez acknowledges a PhD fellowship of the International Max Planck Research School on Physical Processes in the Solar System and Beyond. Vishnu Reddy's research is supported by NASA NEOO Program Grant NNX07AL29G, and NASA Planetary Geology and Geophysics Grant NNX07AP73G. E.A.C. thanks the Canada

Foundation for Innovation, the Manitoba Research Innovations Fund, and the Canadian Space Agency for their support of the establishment of the University of Winnipeg Planetary Spectrophotometer Facility, and NSERC for a Discovery grant, and the University of Winnipeg for various internal grants, to support this project.

## Appendix A. Asteroid spectra

This appendix contains the spectra of all NEAs analyzed in this study. The numerical designation and the date of the observation (YYMMDD) for each asteroid are given (see Figs. A.13–A.15).

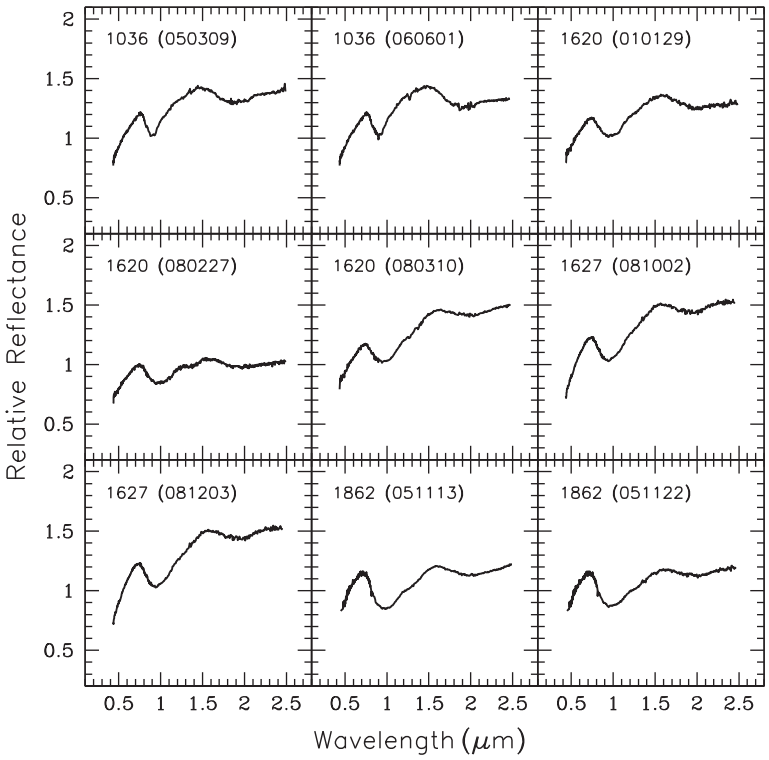


**Fig. A.13.** Reflectance spectra of NEAs analyzed in this study.

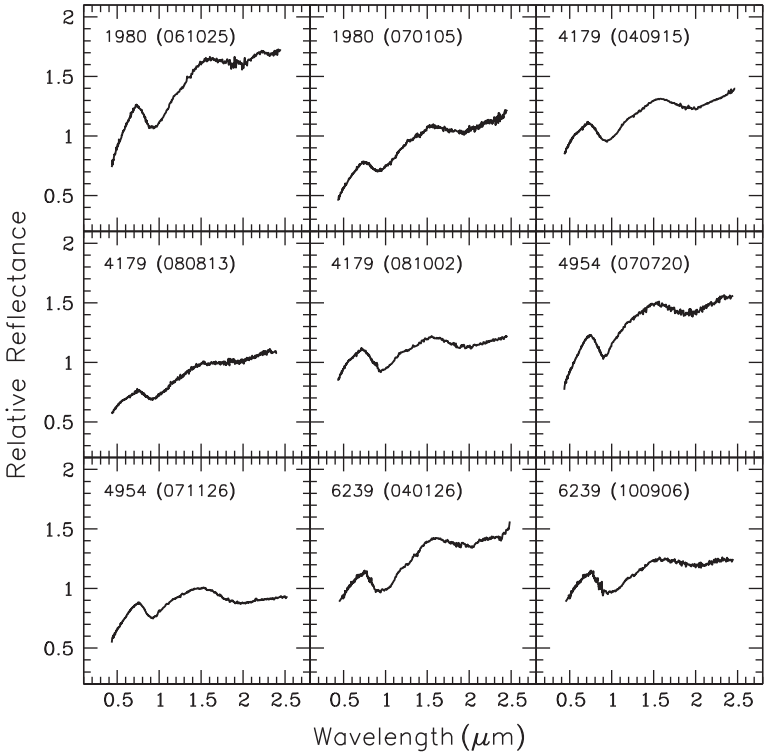


**Fig. A.14.** Reflectance spectra of NEAs analyzed in this study.

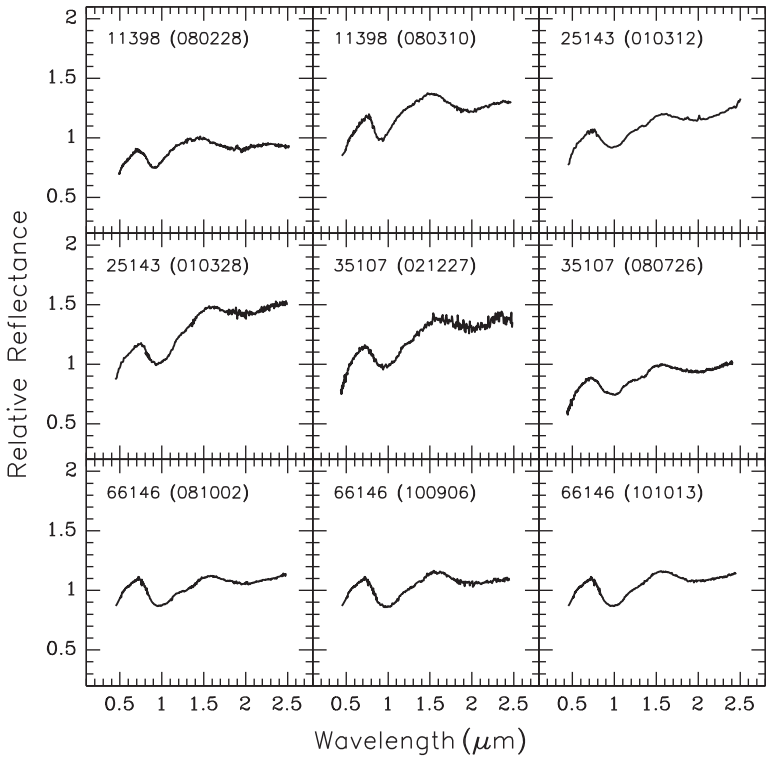


**Fig. A.15.** Reflectance spectra of NEAs analyzed in this study.

## References


Abell, P.A., Vilas, F., Jarvis, K.S., Gaffey, M.J., Kelley, M.S., 2007. Mineralogical composition of (25143) Itokawa 1998 SF36 from visible and near-infrared reflectance spectroscopy: Evidence for partial melting. Meteorit. Planet. Sci. 42, 2165–2177.

Adams, J.B., 1974. Visible and near-infrared diffuse reflectance spectra of pyroxenes as applied to remote sensing of solid objects in the Solar System. J. Geophys. Res. 79, 4829–4836.

Adams, J.B., 1975. Interpretation of visible and near-infrared diffuse reflectance spectra of pyroxenes and other rock-forming minerals. In: Karr, C.I. (Ed.), Infrared and Raman Spectroscopy of Lunar and Terrestrial Minerals. Academic, New York, pp. 91–116.

Adams, J.B., Filice, A.L., 1967. Spectral reflectance 0.4 to 2.0 microns of silicate rock powders. J. Geophys. Res. 72, 5705–5715.

Bell, J.F., Izenberg, N.I., Lucey, P.G., Clark, B.E., Peterson, C., Gaffey, M.J., Joseph, J., Carcich, B., Harch, A., Bell, M.E., Warren, J., Martin, P.D., McFadden, L.A., Wellnitz, D., Murchie, S., Winter, M., Veverka, J., Thomas, P., Robinson, M.S., Malin, M., Cheng, A., 2002. Near-IR reflectance spectroscopy of 433 Eros from the NIS instrument on the NEAR mission: I – Low phase angle observations. Icarus 155, 119–144.

Binzel, R.P., Rivkin, A.S., Bus, S.J., Sunshine, J.M., Burbine, T.H., 2001. MUSES-C target Asteroid (25143) 1998 SF36: A reddened ordinary chondrite. Meteorit. Planet. Sci. 36, 1167–1172.

Binzel, R.P., Rivkin, A.S., Stuart, J.S., Harris, A.W., Bus, S.J., Burbine, T.H., 2004. Observed spectral properties of near-Earth objects: Results for population distribution, source regions, and space weathering processes. Icarus 170, 259–294.

Britt, D.T., Consolmagno, G.J., 2003. Stony meteorite porosities and densities: A review of the data through 2001. Meteorit. Planet. Sci. 38, 1161–1180.

Brunetto, R., Strazzulla, G., 2005. Elastic collisions in ion irradiation experiments: A mechanism for space weathering of silicates. Icarus 179, 265–273.

Brunetto, R., Vernazza, P., Marchi, S., Birlan, M., Fulchignoni, M., Orofino, V., Strazzulla, G., 2006. Modeling asteroid surfaces from observations and irradiation experiments: The case of 832 Karin. Icarus 184, 327–337.

Burbine, T.H., McCoy, T.J., Jaresowich, E., Sunshine, J.M., 2003. Deriving asteroid mineralogies from reflectance spectra: Implications for the MUSES-C target asteroid. Antarct. Meteorite Res. 16, 185–195.

Burbine, T.H., Buchanan, P.C., Binzel, R.P., 2007. Deriving formulas from HED spectra for determining the pyroxene mineralogy of Vesta and Vestoids. Lunar Planet. Sci. 2117 (abstract).

Burbine, T.H., Buchanan, P.C., Dolkar, T., Binzel, R.P., 2009. Pyroxene mineralogies of near-Earth Vestoids. Meteorit. Planet. Sci. 44, 1331–1341.

Burns, R.G., 1993. Mineralogical Applications of Crystal Field Theory. Cambridge University Press, Cambridge, UK, 575pp..

Bus, S.J., Binzel, R.P., 2002a. Phase II of the small main-belt asteroid spectroscopic survey a feature-based taxonomy. Icarus 158, 146–177.

Bus, S.J., Binzel, R.P., 2002b. Phase II of the small main-belt asteroid spectroscopic survey the observations. Icarus 158, 106–145.

Bus, S.J., Vilas, F., Barucci, M.A., 2002. Visible-wavelength spectroscopy of asteroids. In: Bottke, W., Cellino, A., Paolicchi, P., Binzel, R. (Eds.), Asteroids III. University of Arizona Press, pp. 169–182.

Clark, B.E., Hapke, B., Pieters, C., Britt, D., 2002a. Asteroid space weathering and regolith evolution. In: Bottke, W., Cellino, A., Paolicchi, P., Binzel, R. (Eds.), Asteroids III. University of Arizona Press, pp. 585–599.

Clark, B.E., Helfenstein, P., Bell, J.F., Peterson, C., Veverka, J., Izenberg, N.I., Domingue, D., Wellnitz, D., McFadden, L., 2002b. NEAR infrared spectrometer photometry of Asteroid 433 Eros. Icarus 155, 189–204.

Cloutis, E.A., Gaffey, M.J., Jackowski, T.L., Reed, K.L., 1986. Calibrations of phase abundance, composition, and particle size distribution for olivine–orthopyroxene mixtures from reflectance spectra. J. Geophys. Res. 91, 11641–11653.

Cushing, M.C., Vacca, W.D., Rayner, J.T., 2004. Spextool: A spectral extraction package for SpeX, a 0.8–5.5 micron cross-dispersed spectrograph. Publ. Astron. Soc. Pacific 116, 362–376.

DeMeo, F.E., Binzel, R.P., Slivan, S.M., Bus, S.J., 2009. An extension of the Bus asteroid taxonomy into the near-infrared. Icarus 202, 160–180.

DeMeo, F.E., Carry, B., Marchis, F., Birlan, M., Binzel, R.P., Bus, S.J., Descamps, P., Nedelcu, A., Busch, M., Bouy, H., 2011. A spectral comparison of (379) Huenna and its satellite. Icarus 212, 677–681.

Dunn, T.L., McCoy, T.J., Sunshine, J.M., McSween, H.Y., 2010. A coordinated spectral, mineralogical, and compositional study of ordinary chondrites. Icarus 208, 789–797.

Filippenko, A.V., 1982. The importance of atmospheric differential refraction in spectrophotometry. Publ. Astron. Soc. Pacific 94, 715–721.

Gaffey, M.J., 2003. Observational and data reduction techniques to optimize mineralogical characterizations of asteroid surface materials. In: Mackwell, S., Stansbery, E. (Eds.), Lunar and Planetary Institute Science Conference, p. 1602 (abstract).

Gaffey, M.J., 2010. Space weathering and the interpretation of asteroid reflectance spectra. Icarus 209, 564–574.

Gaffey, M.J., Burbine, T.H., Piatek, J.L., Reed, K.L., Chaky, D.A., Bell, J.F., Brown, R.H., 1993. Mineralogical variations within the S-type asteroid class. Icarus 106, 573–602.

Gaffey, M.J., Cloutis, E.A., Kelley, M.S., Reed, K.L., 2002. Mineralogy of asteroids. In: Bottke, W., Cellino, A., Paolicchi, P., Binzel, R. (Eds.), Asteroids III. University of Arizona Press, pp. 183–204.

Gehrels, T., 1970. Photometry of asteroids. In: Dollfus, A. (Ed.), Surfaces and Interiors of Planets and Satellites. Academic Press, London, pp. 317–375.

Gradie, J., Veverka, J., 1986. The wavelength dependence of phase coefficients. Icarus 66, 455–467.

Gradie, J., Veverka, J., Buratti, B., 1980. The effects of scattering geometry on the spectrophotometric properties of powdered material. In: Bedini, S.A. (Ed.), Lunar and Planetary Science Conference Proceedings. Pergamon Press, Newyork, pp. 799–815.
Hapke, B., 1981. Bidirectional reflectance spectroscopy: I – Theory. J. Geophys. Res. 86, 3039–3054.
Hapke, B., 1993. Theory of Reflectance and Emittance Spectroscopy. Cambridge University Press, Cambridge, UK.
Hapke, B., 2001. Space weathering from Mercury to the asteroid belt. J. Geophys. Res. 106, 10039–10074.
Hardersen, P.S., Gaffey, M.J., Cloutis, E.A., Abell, P.A., Reddy, V., 2006. Near-infrared spectral observations and interpretations for S-asteroids 138 Tolosa, 306 Unitas, 346 Hermentaria, and 480 Hansa. Icarus 181, 94–106.
Hinrichs, J.L., Lucey, P.G., 2002. Temperature-dependent near-infrared spectral properties of minerals, meteorites, and lunar soil. Icarus 155, 169–180.
Johnson, P.B., Christy, R.W., 1974. Optical constants of transition metals: Ti, V, Cr, Mn, Fe, Co, Ni, and Pd. Phys. Rev. B 9, 5056–5070.
Kitazato, K., Clark, B.E., Abe, M., Abe, S., Takagi, Y., Hiroi, T., Barnouin-Jha, O.S., Abell, P.A., Lederer, S.M., Vilas, F., 2008. Near-infrared spectrophotometry of Asteroid 25143 Itokawa from NIRS on the Hayabusa spacecraft. Icarus 194, 137–145.
Lumme, K., Bowell, E., 1981. Radiative transfer in the surfaces of atmosphereless bodies: I – Theory. II – Interpretation of phase curves. Astron. J. 86, 1694–1721.
Luu, J.X., Jewitt, D.C., 1990. Charge-coupled device spectra of asteroids: I – Near-Earth and 3:1 resonance asteroids. Astron. J. 99, 1985–2011.
Mann, P., Cloutis, E.A., Reddy, V., 2011. The effect of changing viewing geometry on pyroxene and eucrite reflectance spectra. Lunar Planet. Sci. 2268 (abstract).
Millis, R.L., Bowell, E., Thompson, D.T., 1976. UBV photometry of Asteroid 433 Eros. Icarus 28, 53–67.
Moroz, L., Schade, U., Wäsch, R., 2000. Reflectance spectra of olivine–orthopyroxene-bearing assemblages at decreased temperatures: Implications for remote sensing of asteroids. Icarus 147, 79–93.
Moskovitz, N.A., Willman, M., Burbine, T.H., Binzel, R.P., Bus, S.J., 2010. A spectroscopic comparison of HED meteorites and V-type asteroids in the inner main belt. Icarus 208, 773–788.
Nakamura, T. et al., 2011. Itokawa dust particles: A direct link between S-type asteroids and ordinary chondrites. Science 333, 1113–1116.
Nathues, A., 2000. Spectroscopic Study of Eunomia Asteroid Family. Ph.D. Dissertation, University of Berlin, Germany.
Nathues, A., 2010. Spectral study of the Eunomia asteroid family. Part II: The small bodies. Icarus 208, 252–275.
Noguchi, T. et al., 2011. Incipient space weathering observed on the surface of Itokawa dust particles. Science 333, 1121–1125.
Pieters, C.M. et al., 2000. Space weathering on airless bodies: Resolving a mystery with lunar samples. Meteorit. Planet. Sci. 35, 1101–1107.
Rayner, J.T. et al., 2003. SpeX: A medium-resolution 0.8–5.5 micron spectrograph and imager for the NASA Infrared Telescope Facility. Publ. Astron. Soc. Pacific 115, 362–382.
Reddy, V., 2009. Mineralogical Survey of Near-Earth Asteroid Population: Implications for Impact Hazard Assessment and Sustainability of Life on Earth. Ph.D. Dissertation, University of North Dakota, Grand Forks.
Reddy, V., Sanchez, J.A., Nathues, A., Moskovitz, N.A., Li, J.Y., Cloutis, E.A., Archer, K., Tucker, R.A., Gaffey, M.J., Paul Mann, J., Sierks, H., Schade, U., 2012. Photometric, spectral phase and temperature effects on 4 Vesta and HED meteorites: Implications for the Dawn mission. Icarus 217, 153–168.
Rivkin, A.S., Binzel, R.P., Sunshine, J., Bus, S.J., Burbine, T.H., Saxena, A., 2004. Infrared spectroscopic observations of 69230 Hermes (1937 UB): Possible unweathered endmember among ordinary chondrite analogs. Icarus 172, 408–414.
Schade, U., Wäsch, R., 1999. NIR reflectance spectroscopy of mafic minerals in the temperature range between 80 and 473 K. Adv. Space Res. 23, 1253–1256.
Shepard, M.K., Cloutis, E., 2011. Laboratory measurements of band depth variation with observation geometry. Lunar Planet. Sci. 1043 (abstract).
Shestopalov, D.I., Golubeva, L.F., 2000. Influence of temperature on reflectance spectra of asteroids. Lunar Planet. Sci. 1003 (abstract).
Singer, R.B., Roush, T.L., 1985. Effects of temperature on remotely sensed mineral absorption features. J. Geophys. Res. 901, 12434–12444.
Strazzulla, G., Dotto, E., Binzel, R., Brunetto, R., Barucci, M.A., Blanco, A., Orofino, V., 2005. Spectral alteration of the Meteorite Epinal (H5) induced by heavy ion irradiation: A simulation of space weathering effects on near-Earth asteroids. Icarus 174, 31–35.
Sunshine, J.M., Bus, S.J., McCoy, T.J., Burbine, T.H., Corrigan, C.M., Binzel, R.P., 2004. High-calcium pyroxene as an indicator of igneous differentiation in asteroids and meteorites. Meteorit. Planet. Sci. 39, 1343–1357.
Taylor, L.A. et al., 2001. The effects of space weathering on Apollo 17 mare soils: Petrographic and chemical characterization. Meteorit. Planet. Sci. 36, 285–299.
Tholen, D.J., 1984. Asteroid Taxonomy from Cluster Analysis of Photometry. Ph.D. Thesis, Arizona Univ., Tucson.
Vernazza, P. et al., 2008. Compositional differences between meteorites and near-Earth asteroids. Nature 454, 858–860.